Exact hybrid Vlasov equilibria for sheared plasmas with in-plane and out-of-plane magnetic field

F. Malara, O. Pezzi,* and F. Valentini
Dipartimento di Fisica, Università della Calabria, 87036, Rende (Cosenza), Italy

(Received 21 March 2018; published 31 May 2018)

The hybrid Vlasov-Maxwell system of equations is suitable to describe a magnetized plasma at scales on the order of or larger than proton kinetic scales. An exact stationary solution is presented by revisiting previous results with a uniform-density shear flow, directed either parallel or perpendicular to a uniform magnetic field, and by adapting the solution to the hybrid Vlasov-Maxwell model. A quantitative characterization of the equilibrium distribution function is provided by studying both analytically and numerically the temperature anisotropy and gyrotropy and the heat flux. In both cases, in the shear region, the velocity distribution significantly departs from local thermodynamical equilibrium. A comparison between the time behavior of the usual "fluidlike" equilibrium shifted Maxwellian and the exact stationary solutions is carried out by means of numerical simulations of the hybrid Vlasov-Maxwell equations. These hybrid equilibria can be employed as unperturbed states for numerous problems which involve sheared flows, such as the wave propagation in an inhomogeneous background and the onset of the Kelvin-Helmholtz instability.

DOI: 10.1103/PhysRevE.97.053212

I. INTRODUCTION

Shearing flows in plasma are found in many natural contexts, like, for instance, the interface between the solar wind and planetary magnetospheres (e.g., Refs. [1–3]), the interaction region between fast and slow streams of the solar wind [4], and astrophysical jets [5].

A magnetized plasma configuration with a shearing flow is stable if the jump Δu of the bulk velocity $\mathbf{u}$ across the shear is lower than a certain threshold, which is typically on the order of the background Alfvén velocity component parallel to $\mathbf{u}$ [6]. In this case, waves possibly propagating in the plasma are affected by the velocity shear through different effects. In particular, small scales can be progressively generated in the wave pattern in the direction of the bulk velocity gradient by a phase-mixing mechanism; this effect is similar to phase mixing of Alfvén waves which propagate in a static background with an inhomogeneous Alfvén speed profile (e.g., Refs. [7,8]). The formation of structures at increasingly smaller scales can locally change the nature of waves [9–11], for instance, converting an Alfvén wave into a kinetic Alfvén wave [10–14]. Finally, the inhomogeneity associated with the shear couples propagating modes, generating energy transfers among different kind of waves [13].

In the opposite case of sufficiently large Δu (or small parallel magnetic field), a shearing flow in a plasma is unstable and undergoes the Kelvin-Helmholtz (KH) instability [6], which leads to the formation of vortices located at the shear layer. The dynamics can be more complex in configurations where one component of the magnetic field changes sign across the shear layer [15–18], which generates an interplay between KH instability and magnetic reconnection. When the width of the shear layer becomes of the order of the ion inertial length, dispersive effects can modify the properties of the KH instability [19]. The presence of KH vortices has been revealed all along the flanks of the low-latitude Earth magnetopause [3,20–22] (see also [23] for a review of the KH instability in the magnetosphere context). Moreover, the development of a mixed KH-tearing mode instability has been considered to take place in cometary plasma tails [24]. At large Reynolds numbers, KH instability can become a source of turbulence through nonlinear interactions among vortices or secondary instabilities [25–31]. As an observational example, we can mention a turbulent layer observed in the Earth's magnetopause [32], where KH vortices form as a consequence of the solar wind motion relative to the magnetosphere. It is worth highlighting that, in this environment, the background magnetic field of the Earth can be nearly perpendicular to the sheared flow, due to the slipping of the solar wind over the magnetosphere plasma.

From a theoretical point of view, prior to the study of either wave evolution or KH instability in shearing-flow plasma, there is the problem of setting up a stationary configuration with a shear flow, where the above-mentioned phenomena can occur. This topic does not present any difficulty in the framework of magnetohydrodynamics (MHD), where a large variety of stationary flows can be envisaged, provided that a null total force acts on the magnetofluid at all positions. In contrast, the situation is totally different in the framework of a kinetic theory. In fact, building up a stationary particle distribution function (DF) representing a shear flow in the presence of a background magnetic field represents a nontrivial problem. Such an issue is particularly relevant in contexts where the width of the shear layer is of the order of typical kinetic scales, such as the ion inertial length or Larmor radius. Indeed, in these cases, kinetic aspects become relevant and can affect some properties of the stationary configuration, like profiles of the bulk flow, temperature, heat flux, etc., modifying them with respect to what can be deduced from fluid approaches. For instance, this

*oreste.pezzi@fis.unical.it

is the typical situation which is encountered when one tries to model the shear flow at the Earth's magnetopause [23].

The problem of deducing a stationary configuration with a shear flow for a magnetized plasma within a kinetic description has received certain attention in the literature. In the case of uniform magnetic field, Cai *et al.* [33] have deduced a set of stationary ion distribution functions giving origin to one-dimensional (1D) shear flows directed perpendicularly to the magnetic field. In particular, they have pointed out a different behavior that is found according to the orientation of the flow vorticity with respect to the magnetic field. A similar topic has been treated by other authors: In the uniform **B** case, a form for a stationary shearing kinetic configuration has been deduced within the problem of calculating properties of ion-cyclotron modes [34,35]; the same problem has been considered in the nonuniform **B** case, deriving a set of specific profiles for bulk velocity and magnetic field [36]. More recently, a form of stationary distribution function has been considered in the case of a nonuniform parallel magnetic field and bulk velocity [37]. In the above approaches, the fully kinetic problem has been considered, calculating the distribution functions of both ions and electrons.

Despite the existence of such results, in many studies of the KH instability a shifted local Maxwellian distribution has been considered as unperturbed plasma state (e.g., Ref. [38]). A shifted Maxwellian has the advantage to be more manageable because it allows us to easily choose profiles of density, bulk velocity, temperature, and magnetic field. On the other hand, at shear scales comparable with ion kinetic scales, a shifted Maxwellian does not represent a stationary state. In fact, initializing the system with a shifted Maxwellian leads to the generation of oscillations [39], whose amplitude becomes larger when decreasing the scale of the shear. Though this aspect could be considered as not relevant in the formation of the final turbulent state, it could somehow affect the linear stage of the instability. Moreover, a shifted Maxwellian does not describe the differences which arise in shears with a different vorticity orientation with respect to the magnetic field [33], as happens in the dusk or dawn flanks of the magnetopause, where the vorticity to magnetic field orientation is reversed.

More importantly, when studying wave propagation in shearing flows, the use of exact stationary states instead of a shifted Maxwellian is crucial. In fact, spurious oscillations associated with a nonexact stationary state would superpose to waves, making it difficult to single out effects due to waves.

When one is interested in describing phenomena at scales comparable with ion scales, a successful approach is represented by the so-called hybrid Vlasov-Maxwell (HVM) model, in which ions are kinetically described while electrons are treated as a massless fluid [40]. It represents a sort of compromise between the usual "MHD-like" coarse-grained fluid description and an exceedingly complex fully kinetic approach. The HVM model has been adopted for describing several phenomena occurring at scales where the kinetic ion physics starts to play a significant role into the plasma dynamics [41–47]. Within the HVM framework, a method to derive ion distribution functions representing approximated kinetic stationary solutions has been recently presented by Cerri *et al.* [39]. It is based on the "extended fluid model approach," which considers finite Larmor radius effects in the determination of the ion pressure tensor, and it has been recently adopted to describe temperature anisotropies due to the shear velocity [48,49]. However, it should be noticed that the solutions proposed by Cerri *et al.* [39] are not exactly stationary, even in the framework of the HVM theory. In fact, oscillations are still present, even if with amplitudes definitely smaller than those recovered in the shifted Maxwellian case.

In the present paper, we derive exact stationary solutions for the set of the HVM equations describing a magnetized plasma with an arbitrary shearing flow **u** profile in two different configurations, namely, with a uniform magnetic field **B** parallel or perpendicular to **u**. The derivation of our solutions is inspired by full kinetic solutions previously obtained in analogous configurations [34,35,37], which have been adapted to the HVM model. In particular, an explicit analytical expression for the solution is found in the parallel **B** case, while in the case of perpendicular **B** the solution is calculated by a numerical procedure which integrates single-particle trajectories. The interest of these solutions is twofold: First, they are exactly stationary, and thus can be safely used as unperturbed states either in wave propagation models and in instability studies; second, due to the properties of the HVM model, they realistically represents situations in which the width of shear layer is of the order of or larger than ion kinetic scales, avoiding the complexity of a fully kinetic treatment.

The plan of the paper is the following: In Sec. II, we introduce the equations of the HVM model; in Secs. III and IV, we derive and discuss the stationary solution in the cases of parallel and perpendicular magnetic fields, respectively; in Sec. V, we present the results of numerical simulations where we analyze the behavior of the solution in comparison with that of a shifted Maxwellian; finally, in Sec. VI, we summarize the results.

II. EQUATIONS OF THE MODEL

We consider a quasineutral magnetized plasma composed of kinetic protons and a massless fluid of isothermal electrons (the current analysis easily extends to heavier ions). We are interested in describing shears occurring at scales larger or comparable with proton kinetic scales, i.e., $l \gtrsim d_p \sim \rho_{Lp}$ and $\tau \gtrsim \Omega_{\rm cp}^{-1}$, where $d_p = V_A/\Omega_{\rm cp}$ is the proton skin depth; $\rho_{Lp} = v_{{\rm th},p}/\Omega_{\rm cp}$ is the proton Larmor radius; $\Omega_{\rm cp} = eB_0/m_p c$ is the proton cyclotron frequency; $V_A = B_0/\sqrt{4\pi n_0 m_p}$ is the Alfvén speed; and $v_{{\rm th},p} = (k_B T_0/m_p)^{1/2}$ is the proton thermal speed. Note that $\beta_p = 2v_{{\rm th},p}^2/V_A^2$; m_p, e, n_0, and T_0 are respectively the proton mass, charge, density, and temperature; while B_0, c, and k_B are the magnetic field typical value, the light speed, and the Boltzmann constant.

At these scales, the proton dynamics is successfully modeled by the hybrid Vlasov-Maxwell (HVM) equations:

$$\frac{\partial f}{\partial t} + \mathbf{v}\cdot\nabla f + \frac{e}{m_p}\left(\mathbf{E} + \frac{\mathbf{v}}{c}\times\mathbf{B}\right)\cdot\frac{\partial f}{\partial \mathbf{v}} = 0, \tag{1}$$

$$\frac{\partial \mathbf{B}}{\partial t} = -c\nabla\times\mathbf{E}; \quad \mathbf{j} = \frac{c}{4\pi}\nabla\times\mathbf{B}, \tag{2}$$

$$\mathbf{E} = -\frac{1}{c}(\mathbf{u}\times\mathbf{B}) + \frac{1}{en}\left(\frac{\mathbf{j}\times\mathbf{B}}{c}\right) - \frac{1}{en}\nabla p_e, \tag{3}$$

where $f = f(\mathbf{x},\mathbf{v},t)$ is the proton distribution function in the phase space $(\mathbf{x},\mathbf{v})$. The electric $\mathbf{E}(\mathbf{x},t)$ and magnetic $\mathbf{B}(\mathbf{x},t)$ fields are respectively determined by the generalized Ohm's law and by the Faraday and Ampere laws, by neglecting the displacement current. In Eqs. (1)–(3), $n(\mathbf{x},t) = \int d^3\mathbf{v} f(\mathbf{x},\mathbf{v},t)$ is the proton number density, $\mathbf{u}(\mathbf{x},t) = \int d^3\mathbf{v}\, \mathbf{v} f(\mathbf{x},\mathbf{v},t)/n(\mathbf{x},t)$ is the proton bulk speed, and $\mathbf{j}(\mathbf{x},t)$ is the current density. Electrons are a massless fluid, whose density is equal to that of ions $n_e = n$ for the quasineutrality condition. The electron pressure p_e is determined by imposing a closure assumption for the electron dynamics (such as isothermal or adiabatic state equation).

Our goal is to build up a stationary hybrid equilibrium state for a sheared flow in the presence of a homogeneous background magnetic field. The shear is directed along y and depends on x, i.e., $\mathbf{u_0} = u_0(x)\mathbf{e}_y$, and spatial variations occur only along x. Two different cases are discussed: (i) magnetic field $\mathbf{B}$ *parallel* to $\mathbf{u_0}$, i.e., $\mathbf{B} = B_0\mathbf{e}_y$; and (ii) magnetic field $\mathbf{B}$ *perpendicular* to $\mathbf{u_0}$, i.e., $\mathbf{B} = B_0\mathbf{e}_z$. These two cases will be investigated separately in the rest of the paper.

In the parallel case, no electric field is needed to set the initial equilibrium and electrons are a massless isothermal fluid: $T_e = \text{const} \rightarrow p_e = k_B n T_e$. In the perpendicular case, an equilibrium electric field, directed along x, is needed to equilibrate the $\mathbf{u_0} \times \mathbf{B}$ term in Eq. (3): $\mathbf{E} = E(x)\mathbf{e}_x$. In this case, we also need to relax the electrons' closure, by treating the electron pressure p_e as a further independent quantity determined by the following equation:

$$\left[\frac{\partial}{\partial t} + (\mathbf{u}_e \cdot \nabla)\right]\left(\frac{p_e}{n^{\gamma_e}}\right) = 0, \tag{4}$$

where γ_e is the electron adiabatic index and $\mathbf{u}_e = \mathbf{u} - \mathbf{j}/n$. Last equation implies that the electron temperature is not homogeneous. Therefore,

$$E(x) = -\frac{u_0 B_0}{c} - \frac{1}{ne}\frac{dp_e}{dx}. \tag{5}$$

The presence of such electric field introduces a charge separation, which in principle is not taken into account within the HVM model ($n_e = n$). However, the discrepancy from the quasineutrality condition is extremely small.

To conclude this section, we remark that the first attempts for modeling a plasma configuration with a velocity shear at kinetic scales essentially extend the fluid equilibrium at smaller scales (e.g., Ref. [38]). These equilibria, based on the local thermodynamical hypothesis [6], assume the following form for the proton VDF (sheared Maxwellian):

$$f_{\mathrm{SM}}(x,\mathbf{v},t) = \frac{n_0}{(2\pi)^{3/2} v_{\mathrm{th},p}^3} \exp\left\{-\frac{v_x^2 + [v_y - u_0(x)]^2 + v_z^2}{2v_{\mathrm{th},p}^2}\right\}, \tag{6}$$

where $\mathbf{v} = (v_x, v_y, v_z)$, n_0 is the proton density, and $\mathbf{u_0} = u_0(x)\mathbf{e}_y$ is the bulk velocity, with $u_0(x)$ being a given function. It can be easily verified that f_{SM} is not a stationary solution of HVM equations in both cases (parallel and perpendicular) discussed above.

In the following, we will revisit and formalize, for the HVM equations, the derivation of kinetic stationary equilibria for a sheared flow by considering two different geometrical configurations. We anticipate that our approach is easier with respect to the ones adopted in previous works [33–37] and implementing our equilibrium in the HVM code is hence quite simple. This allows us to perform hybrid kinetic simulations with a "proper" (and simple) hybrid kinetic equilibrium. We also remark that the sheared Maxwellian DF is often adopted also for analyzing phenomena occurring at kinetic scales in sheared flows, such as KH instability. This choice can be easily justified for the investigation of a particular class of phenomena, where nonlinearities play a crucial role in developing turbulence, such as KH instability (e.g., Ref. [38]). One can correctly argue that, for these processes, the final difference that would occur starting with the sheared Maxwellian or with the "proper" equilibrium DF is minimal and does not affect the final dynamical state. However, for another class of processes (such as phase mixing of a linear wave in a velocity shear [9–14]), starting from a correct equilibrium is crucial for properly investigating the phenomenon itself. In this direction, several works have been focused on extending the MHD-like fluid equilibrium to the microphysics [39,48–51] and our work gives a further contribution in this direction.

III. STATIONARY SOLUTION FOR THE PARALLEL CASE: $\mathbf{u_0} \,||\, \mathbf{B}$

Here we revisit the derivation of the stationary solution of Eqs. (1)–(3), in the case in which velocity shear and homogeneous magnetic field are parallel and the electric field is vanishing. The method we adopt is similar to the Harris approach for deriving kinetic equilibria corresponding to localized current sheets [52] and it is based on the determination of the proton DF as a function of the motion constants, derived from the Lagrangian description of single-particle dynamics. A similar derivation can be found in Ref. [37] in the framework of fully kinetic theory; here, we reconsider the same problem to adapt the solution to the HVM model. Moreover, we discuss in deeper detail the properties of the derived stationary DF, illustrating the spatial profiles of its moments (bulk velocity, temperatures, heat flux).

For the present geometry, the Lagrangian of the single-particle dynamics is

$$\mathcal{L} = \frac{m_p}{2}\left(v_x^2 + v_y^2 + v_z^2\right) - \frac{e}{m_p} v_z B_0 x, \tag{7}$$

where $\mathbf{A} = A_z\mathbf{e}_z = B_0 x\, \mathbf{e}_z$ is the vector potential associated with the magnetic field. From the integrals of motion of $\mathcal{L}$, which are the generalized momenta P_y, P_z and the energy E, we can define three auxiliary constants:

$$\begin{aligned} k_1 &= P_y = m_p v_y \\ k_2 &= -\frac{P_z c}{e B_0} = x - \frac{v_z}{\Omega_{\mathrm{cp}}} \\ k_3 &= E = \frac{m_p}{2}\left(v_x^2 + v_y^2 + v_z^2\right). \end{aligned} \tag{8}$$

To write the proton DF $f_{\mathrm{eq},||}$, we consider the following combinations of the above constants, having the dimension of a velocity, $\alpha_1 = \{\frac{2}{m_p}[E - \frac{P_y^2}{2m_p}]\}^{1/2}$ and $\alpha_2 = \frac{P_y}{m_p} - U(x - \frac{v_z}{\Omega_{\mathrm{cp}}})$, being $U = U(k_2)$ the arbitrary shear, function of the motion integral k_2.

Since α_1 and α_2 are motion integrals, each generic function $F(\alpha_1^2 + \alpha_2^2)$ is a stationary solution of the Vlasov equation [53].

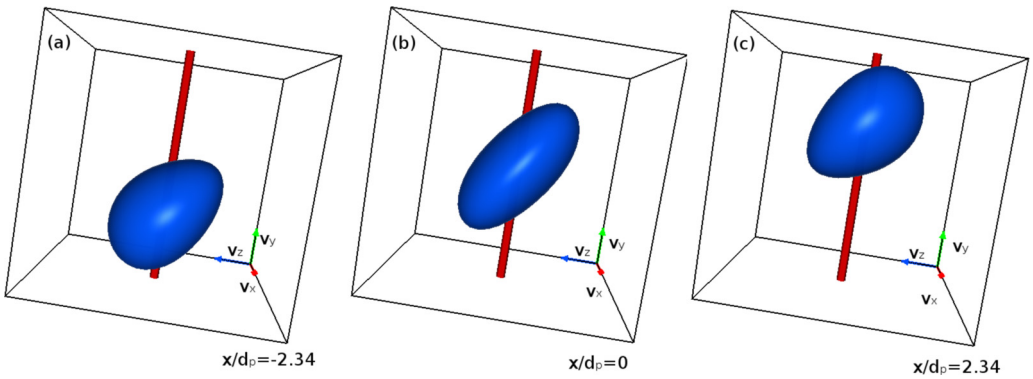

FIG. 1. Isosurface plot of the proton DF $f_{\mathrm{eq},||}$ in velocity space at $x/d_p = -2.34$ (a), $x/d_p = 0$ (b), and $x/d_p = 2.34$ (c). In each panel, red, green, and blue arrows refer to v_x, v_y, and v_z, respectively. The red tube indicates the magnetic field direction.

The function F is determined by imposing that $f_{\mathrm{eq},||}$ reduces to a Maxwellian with density n_0 and thermal speed $v_{\mathrm{th},p}$ in the absence of the shear ($U = 0$), and hence

$$f_{\mathrm{eq},||}(x,\mathbf{v}) = \frac{n_0}{(2\pi)^{\frac{3}{2}} v_{\mathrm{th},p}^3} \exp\left[-\frac{1}{2v_{\mathrm{th},p}^2}\left\{ v_x^2 + \left[v_y - U\left(x - \frac{v_z}{\Omega_{\mathrm{cp}}} \right) \right]^2 + v_z^2 \right\} \right]. \quad (9)$$

This solution is a stationary equilibrium for the HVM set of equations Eqs. (1)–(3), for the case of a shear parallel to the background magnetic field. Indeed, Eqs. (2) and (3) are also exactly satisfied, since the zeroth-order moment of $f_{\mathrm{eq},||}$ gives a homogeneous density n_0 and the bulk speed $\mathbf{u}$ is along y (see the next subsection for further details). The DF $f_{\mathrm{eq},||}$ is a Maxwellian-like function shifted along v_y, in which, however, the amount of the shift depends on both the position x and the velocity v_z (through the argument of $U, k_2 = x - v_z/\Omega_{\mathrm{cp}}$). For the same reason, the bulk speed u_y does not coincide with U in the general case.

A. Properties of the stationary distribution function $f_{\mathrm{eq},||}$

To characterize the physical properties of $f_{\mathrm{eq},||}$, we focus here on its shape in velocity space and on the evaluation of its moments, in particular density, bulk velocity, temperature, and heat flux.

To display the shape of $f_{\mathrm{eq},||}$ in the velocity space, we choose the tanh-like shear profile of U, routinely adopted for investigating the KH instability,

$$U(k_2) = U_0 \tanh\left(\frac{k_2}{\Delta x} \right), \quad (10)$$

where we choose $U_0 = 2V_A$, $\beta_p = 2v_{\mathrm{th},p}^2/V_A^2 = 4$, and Δx is the width of the shear function U. The width of the sheared bulk velocity $\mathbf{u}(x)$ can be different from Δx. By using the latter expression of U, we compute $f_{\mathrm{eq},||}$ in Eq. (9), by discretizing the four-dimensional phase space through $N_x = 512$ grid points in the one-dimensional spatial domain ($x \in [-L/2, L/2]$) and $N_v = 141$ grid points in each velocity direction ($v_j \in [-v_{\max}, v_{\max}]$, being $j = x,y,z$ and $v_{\max} = 7v_{\mathrm{th},p}$), while we chose $L = 50d_p$ and $\Delta x = 2.5d_p$. Figure 1 show the isosurface plots of $f_{\mathrm{eq},||}$ in velocity space at several spatial positions across the shear: $x/d_p = -2.34$ (a), $x/d_p = 0.0$ (b), and $x/d_p = 2.34$ (c). The red tube in Fig. 1 indicates the magnetic field direction. Far from the shear (not explicitly reported), the distribution function is a shifted Maxwellian, while across the shear it becomes significantly stressed, resembling potato-like shapes with non-null heat flux, temperature anisotropy, and agyrotropy with respect to its principal axes.

We also calculate the moments of the DF $f_{\mathrm{eq},||}$. We already anticipated that the density associated with the DF given by Eq. (9) is uniform, i.e., $n(x) = n_0$. The bulk velocity can be easily evaluated, starting from $\mathbf{u}(\mathbf{x}) = \int d^3\mathbf{v}\, \mathbf{v}\, f_{\mathrm{eq},||}(\mathbf{x},\mathbf{v})/n_0$. It can be easily shown that u_x and u_z are null, while u_y is

$$u_y(x) = \frac{1}{(2\pi)^{1/2} v_{\mathrm{th},p}} \int_{-\infty}^{\infty} U\left(x - \frac{v}{\Omega_{\mathrm{cp}}} \right) \exp\left(-\frac{v^2}{2v_{\mathrm{th},p}^2} \right) dv. \quad (11)$$

The bulk velocity $u_y(x)$ associated with $f_{\mathrm{eq},||}$ does not coincide with the function $U(x)$, but rather it is the result of the convolution between U and a Gaussian function.

Despite the inverse process (i.e., the determination of $U(x)$ and of $f_{\mathrm{eq},||}$ for a given profile of the bulk velocity $u_y(x)$) requires the inversion of the convolution in Eq. (11), it is still possible to deduce some simple results. If Δx is the characteristic spatial length of $U(x)$, then $U(x - v/\Omega_{\mathrm{cp}})$ considered as a function of v varies over the scale $\Delta v = \Omega_{\mathrm{cp}} \Delta x$. The Gaussian factor inside the integral of Eq. (11) represents a windowing function selecting a v interval of width $\sim v_{\mathrm{th},p}$; we indicate such a windowing function by

$$W_G(v) = \frac{1}{(2\pi)^{1/2} v_{\mathrm{th},p}} \exp\left(-\frac{v^2}{2v_{\mathrm{th},p}^2} \right). \quad (12)$$

(a) In the large scale limit $\Delta x \gg \rho_{Lp}$, i.e., $\Delta v \gg v_{\mathrm{th},p}$, the profile of the windowing function is relatively unimportant and $W_G(v)$ can be successfully approximated with the simpler square window $W_S(v)$, centered in $v = 0$, with width and amplitude $\sqrt{2\pi}\, v_{\mathrm{th},p}$ and $1/\sqrt{2\pi}\, v_{\mathrm{th},p}$, respectively. $W_G(v)$ and $W_S(v)$ have the same value at $v = 0$ and the same integral in the interval $(-\infty, +\infty)$. Within the approximation $W_G(v) \simeq W_S(v)$, we obtain

$$u_y(x) \simeq \bar{U}(x) = \frac{1}{\sqrt{2\pi}\, \rho_{Lp}} \int_{-\sqrt{\frac{\pi}{2}}\rho_{Lp}}^{\sqrt{\frac{\pi}{2}}\rho_{Lp}} U(x - \xi) d\xi, \quad (13)$$

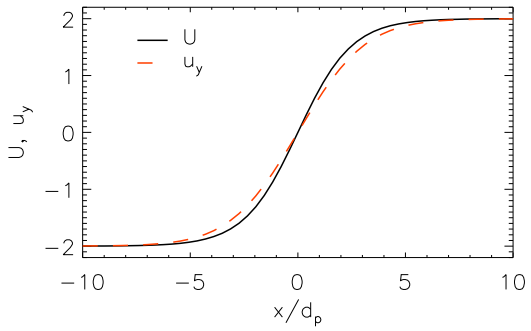

FIG. 2. Initial shear U (black solid) and mean velocity u_y (red dashed), evaluated by the proton DF $f_{\mathrm{eq},||}$, as a function of x across the shear.

which represents the running average of $U(x)$ performed over the interval $[x-\sqrt{\pi/2}\rho_{Lp}, x+\sqrt{\pi/2}\rho_{Lp}]$. In the large-scale limit, the bulk velocity $u_y(x)$ is approximately given by the function $U(x)$ smoothed over an interval of amplitude $\sqrt{2\pi}\rho_{Lp}$ centered at the position x. This result can be easily understood by thinking that the protons' gyromotion in the plane perpendicular to $\mathbf{B}$ mixes up the v_y velocities of the single protons, thus smoothing the profile of $U(x)$ over a length scale which is of the order of the Larmor radius.

(b) In the opposite small-scale limit, i.e., $\Delta x \ll \rho_{Lp}$, Eq. (11) can be rewritten as follows:

$$u_y(x) = \frac{1}{(2\pi)^{1/2}} \int_{-\infty}^{\infty} U(\rho_{Lp}\varphi) \exp\left[-\frac{1}{2}\left(\varphi - \frac{x}{\rho_{Lp}}\right)^2\right] d\varphi, \tag{14}$$

where $\varphi = k_2/\rho_{Lp}$ and $U(\rho_{Lp}\varphi)$ as a function of φ varies on a scale much smaller than unity. If $U(\rho_{Lp}\varphi)$ describes a shear layer corresponding to a bulk velocity which varies in the range $[-U_0, U_0]$, it can be approximated with the Heavyside function $H(\varphi)$:

$$U(\rho_{Lp}\varphi) \simeq U_0 H(\varphi) = \begin{cases} U_0 & \text{if } \varphi > 0 \\ -U_0 & \text{if } \varphi < 0 \end{cases}. \tag{15}$$

After some algebraic steps, Eq. (14) reduces to

$$u_y(x) = \begin{cases} U_0 & \text{if } x \gg \rho_{Lp} \\ -U_0 & \text{if } x \ll -\rho_{Lp} \end{cases}, \quad \text{for } \Delta x \ll \rho_{Lp}, \tag{16}$$

where, for simplifying the integrals, we considered that, for $x \gg \rho_{Lp}$ ($x \ll -\rho_{Lp}$), the Gaussian is essentially located in the positive (negative) part of the φ axis, where $H(\varphi) = 1$ ($H(\varphi) = -1$). Hence, in spite of the small scale of variation of the function $U(x)$ ($\Delta x \ll \rho_{Lp}$), the bulk velocity $u_y(x)$ varies on a scale comparable with the proton Larmor radius ρ_{Lp}. It is not possible to construct, in the current configuration, shear layers with a width smaller than the proton Larmor radius. This is again due to the proton gyromotion, which mixes up the parallel velocity of single particles on a transverse scale of the order of ρ_{Lp}.

To directly display the shape of the bulk velocity, we consider the shear function $U(x)$ [Eq. (10)] and we numerically compute $u_y(x)$, for $\Delta x = 2.5 d_p \simeq 1.77\rho_{Lp}$. Figure 2 reports the spatial profile of the function $U(x)$ (black solid line) and the corresponding bulk velocity u_y (red dashed line). It is clear to note that significant differences between U and u_y are recovered. We also verified that in the large-scale limit the windowing function does not play a significant role and hence $u_y(x) \simeq U(x)$, while in the small-scale limit protons arrange themselves to produce a bulk velocity $u_y(x)$ varying over a scale comparable with the proton Larmor radius; nevertheless, the shear function U varies over scales much smaller than ρ_{Lp} (not reported here).

To further characterize the moments of $f_{\mathrm{eq},||}$, we consider the variance matrix, defined by

$$\sigma_{ij}(x) = \frac{1}{n(x)} \int [v_i - u_i(x)][v_j - u_j(x)] f_{\mathrm{eq},||}(x,\mathbf{v}) d^3\mathbf{v}; \quad i,j = x,y,z, \tag{17}$$

which is related to the proton temperature by $T_0 = m_p \sum_{j=1}^{3} \sigma_{jj}/3k_B$. Since the magnetic field $\mathbf{B}$ is uniform and directed along y, the proton temperatures parallel and perpendicular to $\mathbf{B}$, i.e., in the local $\mathbf{B}$ frame (LBF), are defined, respectively, by $T_{||} = \frac{m_p}{k_B}\sigma_{yy}$ and $T_\perp = \frac{m_p}{k_B}(\sigma_{xx} + \sigma_{zz})/2$, so that $T_0 = (T_{||} + 2T_\perp)/3$.

The analytical evaluation of anisotropy and agyrotropy at the center of a symmetric shear, presented in Appendix A, indicates that the equilibrium DF is anisotropic and agyrotropic. By means of the numerical evaluations of the variance matrix elements, we can extend the analytical computation and consider not only the center of the shear. We numerically diagonalize the matrix σ, thus rotating the DF into the minimum variance frame (MVF). The eigenvalues of σ, corresponding to the temperatures in the MVF, are indicated by $\lambda^{(3)} < \lambda^{(2)} < \lambda^{(1)}$.

The top panel of Fig. 3 shows the temperature anisotropy ratio η and η^*, while the bottom panel indicates the agyrotropy ratio ζ and ζ^*, for the shear $U(x)$ given by Eq. (10) in the case $\Delta x = 2.5 d_p$, both in the MVF (black solid) and in the LBF (red dashed). Temperature anisotropy and agyrotropy have been evaluated as follows: (a) temperature anisotropy in the MVF $\eta = (\lambda_2 + \lambda_3)/2\lambda_1$; (b) temperature anisotropy in the LBF $\eta^* = (\sigma_{xx} + \sigma_{zz})/2\sigma_{yy}$; (c) agyrotropy in the MVF $\zeta = \lambda_3/\lambda_2$; and (d) agyrotropy in the LBF $\zeta^* = \min(\sigma_{xx}, \sigma_{zz})/\max(\sigma_{xx}, \sigma_{zz})$. In the LBF, the DF is anisotropic close to the shear, while no temperature agyrotropies are recovered. On the other hand, in the MVF, the DF displays strong anisotropies as well as agyrotropies close to the velocity shear.

We finally characterize the DF $f_{\mathrm{eq},||}$ by computing the heat flux for unit of mass:

$$q_j(x) = \frac{1}{2} \int [v_j - u_j(x)][\mathbf{v} - \mathbf{u}(x)]^2 f_{\mathrm{eq},||}(x,\mathbf{v}) d^3\mathbf{v}; \quad j = x,y,z, \tag{18}$$

where the shear function $U(x)$ in Eq. (10), with $\Delta x = 2.5 d_p$, is adopted. Figure 4 reports the three components of the heat flux q_x (black solid line), q_y (red dashed line), and q_z (blue dotted line), as a function of x/d_p. The equilibrium DF $f_{\mathrm{eq},||}$ is such that a nonvanishing heat flux is recovered at $x/d_p \simeq 0$ in the two components q_y and q_z, which tends to zero away from the shear.

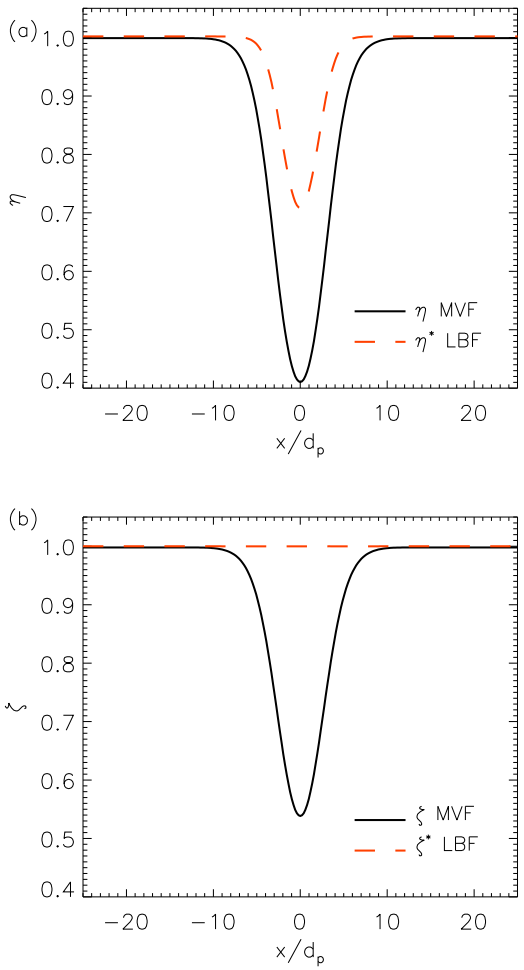

FIG. 3. Temperature anisotropy η, η^* (top) and agyrotropy ζ, ζ^* (bottom) evaluated in the minimum variance frame (black solid) and in the local magnetic field frame (red dashed), associated with the proton DF $f_{\mathrm{eq},||}$.

IV. STATIONARY SOLUTION FOR THE PERPENDICULAR CASE: $\mathbf{u_0} \perp \mathbf{B}$

We revisit here the derivation of the stationary solution of Eqs. (1)–(3), in the case in which velocity shear and homogeneous magnetic field are perpendicular, while the electric field is $\mathbf{E} = E(x)\mathbf{e}_x$. The method here adopted is based on the dynamics of a single proton in the electric $\mathbf{E}$ and magnetic $\mathbf{B}$ fields. Particle trajectories have been already studied to build up a stationary solution in a fully kinetic (ion + electron) description in previous studies [33–35]. In particular, in the analytical description of single-particle dynamics, we follow the same method as Ganguli *et al.* [34], but deriving further general results which are important for setting up our numerical description of particle dynamics. We will also derive a form for the proton distribution function which is different from that in Ref. [34] (except in the particular case of linearly growing electric field). In our case, the derived DF is furthermore supplemented with a form for the electron pressure profile, which allows us to obtain an exact stationary state for the whole set of HVM equations.

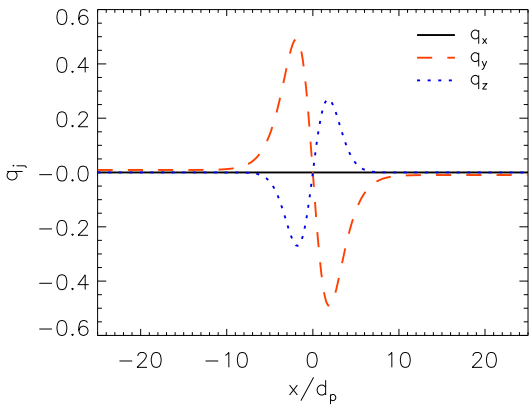

FIG. 4. Heat flux q_x (black solid), q_y (red dashed), and q_z (blue dotted), associated with the proton DF $f_{\mathrm{eq},||}$.

Our derivation starts from considering the single-particle motion. The proton motion along the parallel z direction is decoupled from the motion in the transverse plane. Therefore, we focus on the particle motion in the xy plane, described by

$$\frac{dv_x}{dt} = \Omega_{\mathrm{cp}} v_y + \frac{e}{m_p} E(x), \quad \frac{dv_y}{dt} = -\Omega_{\mathrm{cp}} v_x,$$
$$\frac{dx}{dt} = v_x. \tag{19}$$

The particle motion depends on the electric field profile $E(x)$, which indirectly determines the profile $u(x)$ of the bulk velocity. We consider a situation where $u(x)$ varies, crossing one or more shear layers, but becomes essentially uniform far from the shear layers: $E(x) = E_{+\infty}$ ($E(x) = E_{-\infty}$) for large positive (negative) x. Thus, in the homogeneous region, particles drift along y with a uniform drift velocity $\mathbf{v}_{d,\pm\infty} = c(\mathbf{E}_{\pm\infty} \times \mathbf{B})/B^2$.

From Eqs. (19), it is easy to obtain

$$v_y = -\Omega_{\mathrm{cp}} x + W_0, \tag{20}$$

$$\frac{d^2x}{dt^2} = -\Omega_{\mathrm{cp}}^2 x + \frac{e}{m_p} E(x) + \Omega_{\mathrm{cp}} W_0, \tag{21}$$

where W_0 is a constant determined by initial conditions and Eq. (21) is a nonlinear oscillator equation for $x(t)$. We integrate Eq. (21) in the interval $[x_0,x]$, by considering that $dv_x/dt = d/dx(v_x^2/2)$ and by rewriting $v_{0y} = W_0 - \Omega_{\mathrm{cp}} x_0$ (being x_0 an arbitrary position corresponding to v_{0y}):

$$\tfrac{1}{2} m_p v_x^2 + e\phi(x) + \tfrac{1}{2} m_p \Omega_{\mathrm{cp}}^2 (x - x_0)^2$$
$$- m_p \Omega_{\mathrm{cp}} v_{0y} (x - x_0) = e_0, \tag{22}$$

where $\phi(x) = -\int_{x_0}^{x} E(x')dx'$ is the electrostatic potential, which vanishes at $x = x_0$, and $e_0 = m_p v_{x0}^2/2$ is a constant, v_{x0} being the value of v_x at $x = x_0$.

Equation (22) expresses the energy conservation for a particle with mass m_p following a 1D motion in the effective potential energy $U_{\mathrm{eff}}(x) = U_E(x) + U_\Omega(x)$, where $U_E(x) =$

$e\phi(x)$ is the electrostatic potential energy and

$$U_\Omega(x) = \frac{1}{2}m_p\Omega_{\rm cp}^2(x-x_0)^2 - m_p\Omega_{\rm cp}v_{0y}(x-x_0) = \frac{1}{2}m_p\Omega_{\rm cp}^2\left(x-\frac{W_0}{\Omega_{\rm cp}}\right)^2 + \frac{1}{2}m_p v_{0y}^2. \quad (23)$$

The term $U_\Omega(x)$ hence corresponds to an attractive force toward the position $W_0/\Omega_{\rm cp}$.

For large $|x-x_0|$, the term $U_\Omega(x)$ dominates in the determining the effective potential energy $U_{\rm eff}(x)$. Indeed, since $E(x)$ becomes constant for sufficiently large values of $|x-x_0|$, we have that $U_E \simeq -E_{+\infty}(x-x_0)$ [$U_E \simeq -E_{+\infty}(x-x_0)$] for large positive (negative) values of $x-x_0$, while $U_\Omega(x)$ is quadratic with respect to $(x-x_0)$. The motion of the particle along x is hence confined inside a potential well: $x_m \leqslant x(t) \leqslant x_M$, where $U_{\rm eff}(x_m) = U_{\rm eff}(x_M) = e_0$ and the particle moves back and forth in the interval $[x_m, x_M]$, with vanishing v_x at x_m and x_M. In other words, $x(t)$ and $v_x(t)$ are periodic function with period τ and, from Eq. (20), follows that $v_y(t)$ is also periodic with period τ. Therefore, the particle follows a closed trajectory in the $v_x v_y$ plane. Notice that $y(t)$ is not necessarily a periodic function and the particle trajectory in the xy plane is, in general, an open curve. The details of the motion along x, like the period τ, depend both on the specific form of the electric field profile $E(x)$ and on the particle initial conditions, which determine the constant quantity W_0. However, the periodicity of variables $x(t)$, $v_x(t)$, and $v_y(t)$ holds for any form of $E(x)$ and for any initial condition. This result is crucial for the setup of the numerical method we employed to calculate a stationary proton DF $f_{{\rm eq},\perp}$ for an arbitrary electric field profile.

Since the particle motion in the $v_x v_y$ plane is periodic, the time average of the velocity over the period τ provides the drift velocity in the particle motion. Therefore, we define the guiding center velocity $\mathbf{v}_c$ as

$$\mathbf{v}_c = \langle \mathbf{v} \rangle_\tau = \frac{1}{\tau}\int_0^\tau \mathbf{v}(t)\,dt. \quad (24)$$

The x component of the guiding center velocity is trivially vanishing; hence, $\mathbf{v}_c = v_{cy}\mathbf{e}_y = \langle v_y \rangle_\tau \mathbf{e}_y$. We also define the *guiding center position* x_c as the position where the particle velocity component v_y is equal to the guiding center velocity: $v_y = v_{cy}$; hence, from Eq. (20), we find

$$x_c = (W_0 - v_{cy})/\Omega_{\rm cp}. \quad (25)$$

Note that (i) Eq. (25) implies that a single value is admitted for x_c and (ii) the guiding center position x_c represents also the time-averaged particle x position: $x_c = \langle x \rangle_\tau$.

We point out that our particle guiding center definition is different from that used in previous studies. In fact, in Refs. [33,54], the guiding center position is defined as a point where $v_y = u_y$, implying that a given particle can have more than one guiding center (see Ref. [33] for a discussion). In contrast, in our approach a single guiding center is defined for each particle, regardless of the specific electric field profile $E(x)$ and the particle initial condition. In Ref. [34], the guiding center position is defined as the position where the effective potential energy is minimum. Also, this definition differs from ours, except for particular profiles of the linearly growing electric field (see Appendix B).

To build the stationary DF for the HVM Eqs. (1)–(3), we consider the particle total energy, which is a constant of motion:

$$\mathscr{E} = K + U_E' = \tfrac{1}{2}m_p\left(v_x^2 + v_y^2 + v_z^2\right) + U_E', \quad (26)$$

where the electric potential energy $U_E'(x)$ is redefined such that $U_E'(x_c) = 0$; i.e., it vanishes at the guiding center position x_c of the considered particle $U_E'(x) = -e\int_{x_c}^x E(x')\,dx'$. This choice can be justified by the following argument. Let us consider the particular case of a uniform electric field $E(x) = E_0$, corresponding to proton circular orbits in the $v_x v_y$ plane, with uniform drift velocity $v_{cy} = -cE_0/B$. In such a case, the potential energy has the form $U_E'(x) = -eE_0(x-x_c)$. Since $x_c = \langle x \rangle_\tau$, it follows that $\langle U_E' \rangle_\tau = 0$; i.e., it has the same value for all particles, regardless of their average position x_c. This is in accordance with the macroscopic invariance of fluid properties with x, which characterizes this particular case. In contrast, a potential energy U_E which vanishes at a fixed position x_0 (equal for all the particles) would give $\langle U_E \rangle_\tau = eE_0(x_c - x_0)$, i.e., an average potential energy which systematically varies with the average position x_c of particles.

We define also the quantity $\mathscr{E}_0 = \mathscr{E} - m_p v_{cy}^2/2$ which represents the part of the particle energy not due to the drifting motion. Of course, $\mathscr{E}_0$ is another motion constant. Since $\mathscr{E}$ is constant, its value can be evaluated at $x = x_c$, where $U_E'(x_c) = 0$ and where, by definition, $v_y = v_{cy}$. Thus,

$$\mathscr{E} = \tfrac{1}{2}m_p\left\{[v_x(x=x_c)]^2 + v_z^2\right\} + \tfrac{1}{2}m_p v_{cy}^2, \quad (27)$$

implying

$$\mathscr{E}_0 = \tfrac{1}{2}m_p\left\{[v_x(x=x_c)]^2 + v_z^2\right\}. \quad (28)$$

To understand how to define the proton DF, we again consider the particular case of constant electric field and we require that, in this case, the DF is a shifted Maxwellian:

$$f_{\rm SM}(\mathbf{v}) = C\exp\left[-\frac{v_x^2 + (v_y - v_{cy})^2 + v_z^2}{2v_{{\rm th},p}^2}\right], \quad (29)$$

where $v_{{\rm th},p}$ is the thermal speed and C is a normalization constant. The uniform-E case analyzed above can be also reproduced in the local approximation description, whose details are reported in Appendix B, by setting $\alpha_0 = 0$ ($\omega^2 = \Omega_{\rm cp}^2$), which implies that $v_x^2 + (v_y - v_{cy})^2 = [v_x(x=x_c)]^2$. Therefore, in this case, by comparing Eqs. (28) and (29), we conclude that

$$f_{\rm SM}(\mathbf{v}) = C\exp\left(-\frac{\mathscr{E}_0}{m_p v_{{\rm th},p}^2}\right). \quad (30)$$

The above considerations lead us to the following "ansatz": We hypothesize that a stationary proton DF representing a shearing flow for *any* electric field profile $E(x)$ can have the following implicit form:

$$f_{{\rm eq},\perp}(x,\mathbf{v}) = C\exp\left[-\frac{\mathscr{E}_0(x,v_x,v_y,v_z)}{m_p v_{{\rm th},p}^2}\right], \quad (31)$$

where $\mathscr{E}_0(x,v_x,v_y,v_z) = \mathscr{E} - m_p v_{cy}^2/2$ is the single-proton energy not due to the drifting motion. As showed above, Eq. (31) is a shifted Maxwellian for an uniform electric field.

Of course, such a conjecture must be verified *a posteriori*. This can be done first in the particular case of the local

approximation, reported in Appendix B, where we also derive the explicit form of the equilibrium DF. Then, in the case of a generic electric field profile $E(x)$ the same quantities will be calculated by employing a numerical technique. It is important to highlight that, since the quantity $\mathscr{E}_0$ is a constant of the particle motion, $f_{\mathrm{eq},\perp}$ is a stationary solution of the Vlasov equation [Eq. (1)], provided that both the electric and magnetic fields are temporally constant [53].

The numerical method employed to generate the equilibrium DF $f_{\mathrm{eq},\perp}$, for a generic electric field profile $E(x)$, is described in the following. We assume that $f_{\mathrm{eq},\perp}$ has the form given by Eq. (31), being

$$\mathscr{E}_0(x,v_x,v_y,v_z) = \frac{m_p}{2}\left(v_x^2+v_y^2+v_z^2\right) + U'_E(x,v_x,v_y) - \frac{m_p}{2}v_{cy}^2(x,v_x,v_y). \tag{32}$$

Here, $v_{cy}^2(x,v_x,v_y)$ indicates the guiding center velocity of a particle which is located at the position x, with velocity (v_x,v_y) at a given time t, while $U'_E(x,v_x,v_y)$ is the electric potential of the same particle. Since $\mathscr{E}_0$ is a motion constant, the time t when $\mathscr{E}_0$ is evaluated can be arbitrarily chosen. Hence, in Eq. (32), (x,v_x,v_y,v_z) can be interpreted as the position and velocity of a single particle at the initial time of its motion. The evaluation of the last two terms in Eq. (32) requires us, however, to integrate the single-particle motion in Eqs. (19). This has been done by the following numerical procedure:

(i) We consider a 1D-3V phase space, composed of a spatial coordinate $x \in [0,L]$, discretized with N_x grid points, and three velocity coordinates $v_m \in [-v_{\max},v_{\max}]$ $m = x,y,z$, discretized with N_v grid points along each direction. We numerically integrate $N_x \times N_v^2$ particle motion Eqs. (19), using each point $(x_i,v_{x,j},v_{y,k})$ of the subgrid as initial condition: $x(t=0)=x_i$, $v_x(t=0)=v_{x,j}$, $v_y(t=0)=v_{y,k}$ (i,j,k are indexes which span along x, v_x, and v_y, respectively). The v_z component, whose index is l, is neglected since the motion is trivial along z. The time integration of Eqs. (19) has been carried out through a third-order Adam-Bashforth scheme, with the time step Δt chosen to maintain the CFL condition.

(ii) Since the exact trajectories in the v_xv_y plane are necessarily closed, each integration is stopped when the corresponding orbit in the v_xv_y plane is completed. The corresponding time T represents the orbit period.

(iii) We calculate, for each orbit, the velocity and x position of the guiding center: $v_{cy,ijk} = \langle v_y\rangle_T$ and $x_{c,ijk} = \langle x\rangle_T$. The electric potential associated with the particle initial position is calculated as $\phi_{ijk} = -\int_{x_{c,ijk}}^{x_i} E(x)\,dx$, where the integral is numerically evaluated. Then, the DF at a given point of the phase space is evaluated as

$$f_{\mathrm{eq},\perp}(x_i,v_{x,j},v_{y,k},v_{z,l}) = C\exp\left[-\frac{1}{2v_{\mathrm{th},p}^2}\left(v_{x,j}^2+v_{y,k}^2+v_{z,l}^2 - v_{yc,ijk}^2\right) - \frac{e\phi_{ijk}}{m_p v_{\mathrm{th},p}^2}\right]. \tag{33}$$

From this expression, the moments of the distribution function (density, temperatures, bulk velocity, and heat flux components) are numerically evaluated. In particular, all the moments vary only in the x direction and the bulk velocity $\mathbf{u}(x)$ is directed in the y direction.

(iv) The resulting $u_y(x)$ depends on the chosen profile of the electric field $E(x)$. However, for an arbitrary electric field profile $E(x)$, the bulk velocity does not coincides with the local $\mathbf{E}\times\mathbf{B}$ drift velocity. On the other hand, $\mathbf{E}$ and $\mathbf{u}$ appear in the generalized Ohm's law (3), which must be consistently satisfied. This is obtained by choosing a profile for the electron pressure $p_e(x)$ such that

$$\frac{dp_e}{dx} = -qn(x)\left[\frac{Bu_y(x)}{c}+E(x)\right] \tag{34}$$

Then, in the general case the electron pressure p_e is not uniform, except in the case of a linear electric field profile (see Appendix B). By adopting this closure for the electron pressure, it is easy to show that the considered configuration is a stationary solution of the whole set of HVM Eqs. (1)–(3) supplemented by Eq. (4) for the electron pressure.

A. Properties of the stationary distribution function $f_{\mathrm{eq},\perp}$

To analyze the properties of the equilibrium DF $f_{\mathrm{eq},\perp}$, we focus on the following shape for the electric field:

$$E_x(x) = -E_0\tanh\left(\frac{x}{\Delta x}\right), \tag{35}$$

representing a shear layers of amplitude $E_0 = 1$ (in scaled unit) and width $\Delta x = 2.5d_p$. By using the latter expression of $E_{0,x}$, we compute $f_{\mathrm{eq},\perp}$ in Eq. (31), by discretizing the four-dimensional phase space through $N_x = 512$ grid points in the one-dimensional spatial domain ($x\in[-L/2,L/2]$) and $N_v = 141$ grid points in each velocity direction ($v_j \in [-v_{\max},v_{\max}]$, being $j=x,y,z$ and $v_{\max} = 7v_{\mathrm{th},p}$), while we chose $L = 50d_p$ and $\Delta x = 2.5d_p$. It is worth noting that the difference between the electric field from which we compute the equilibrium [Eq. (35)] and the term $-\mathbf{u}\times\mathbf{B}/c$ evaluated using the equilibrium DF mean speed is of the order of 10^{-5}. Although this quantity is small at the initial time, one needs to take care of it by self-consistently solving Eq. (4) to maintain the equilibrium.

Figure 5 reports the isocontour of the proton DF $f_{\mathrm{eq},\perp}$ in the velocity space. Figures 5(a) to 5(c) refer to different positions across the shear: $x/d_p = -2.34$ (a), $x/d_p = 0.0$ (b), and $x/d_p = 2.34$ (c). The red tube in Fig. 5 indicates the magnetic field direction. We note that, against the parallel case, here the equilibrium DF is less stressed and exhibits a bi-Maxwellian-like structure, elongated in a direction transverse to the magnetic field direction. As for the parallel case, far from the shear, the DF $f_{\mathrm{eq},\perp}$ reduces to the shifted Maxwellian, while—across the shear—it exhibits a clear temperature anisotropy.

Figure 6 reports the temperature anisotropy (top panel) and agyrotropy (bottom panel) ratios both in the MVF (black solid) and in the LBF (red dashed). Temperature anisotropy and agyrotropy have been evaluated as follows: (a) temperature anisotropy in the MVF $\eta = (\lambda_2+\lambda_3)/2\lambda_1$; (b) temperature anisotropy in the LBF $\eta^* = (\sigma_{xx}+\sigma_{yy})/2\sigma_{zz}$; (c) agyrotropy in the MVF $\zeta = \lambda_3/\lambda_2$; and (d) agyrotropy in the LBF $\zeta^* = \min(\sigma_{xx},\sigma_{yy})/\max(\sigma_{xx},\sigma_{yy})$. Note that the definitions in the LBF are different from the parallel case, since the orientation of the magnetic field has been changed. If in the parallel case the equilibrium distribution function was characterized by stronger anisotropies in the MVF frame, here the situation is

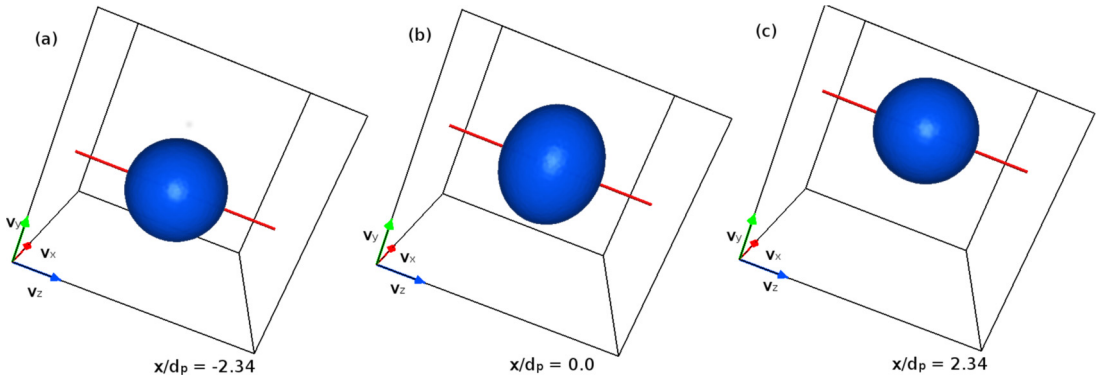

FIG. 5. Isosurface plot of the proton DF $f_{\mathrm{eq},\perp}$ in velocity space at $x/d_p = -2.34$ (a), $x/d_p = 0$ (b), and $x/d_p = 2.34$ (c). In each panel, red, green, and blue arrows refer to v_x, v_y, and v_z, respectively. The red tube indicates the magnetic field direction.

the opposite. Indeed, in the MVF, the DF is strongly anisotropic at the shear, but it does not present significant nongyrotropic features. On the other hand, in the LBF frame, the DF is significantly anisotropic as well agyrotropic.

Finally, we characterize the DF by evaluating the heat flux [Eq. (18)]. Figure 7 reports the three components of the heat flux q_x (black solid line), q_y (red dashed line), and q_z (blue dotted line), as a function of x/d_p. Clearly, a nonvanishing heat flux is recovered at $x/d_p \simeq 0$ in the y component.

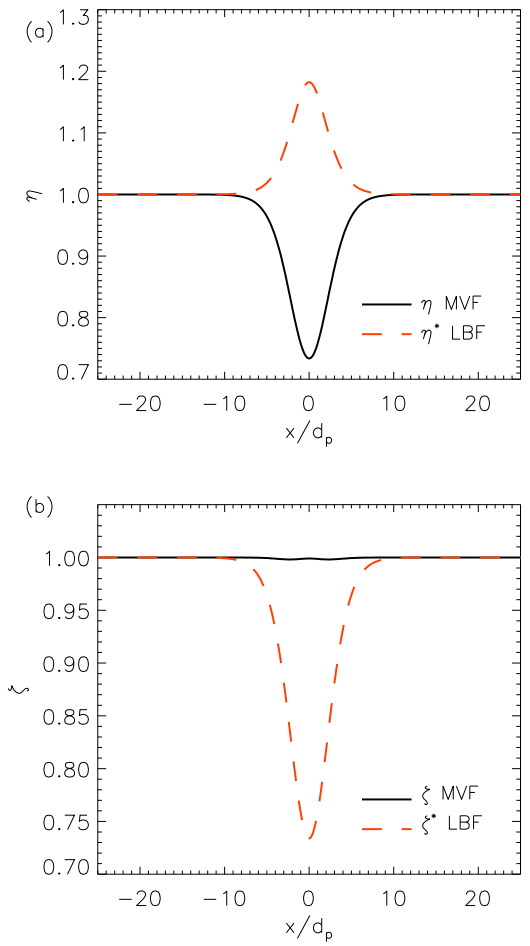

FIG. 6. Temperature anisotropy η, η^* (top) and agyrotropy ζ, ζ^* (bottom) evaluated in the minimum variance frame (black solid) and in the local magnetic field frame (red dashed), associated with the proton DF $f_{\mathrm{eq},\perp}$.

V. HYBRID VLASOV-MAXWELL SIMULATIONS OF THE EQUILIBRIUM

In this section, we numerically test that distribution functions derived in the previous sections $f_{\mathrm{eq},\parallel}$ and $f_{\mathrm{eq},\perp}$ are effectively stationary equilibria for the HVM set of equation, which are solved numerically in the so-called HVM code [40,55–59], by also comparing these equilibria with the sheared Maxwellian case f_{SM}.

The HVM code solves numerically the set of Eqs. (1)–(4) in dimensionless form through a Eulerian algorithm described in detail in Ref. [40]. In the parallel case, since T_e is homogeneous and constant, Eq. (4) is trivial. Dimensionless HVM equations are obtained by scaling velocities by the Alfvén speed V_A, lengths by the proton skin depth d_p, and time by the inverse proton cyclotron frequency $\Omega_{\mathrm{cp}}^{-1}$. Since the problem is intrinsically one-dimensional in physical space, we restrict our numerical runs to a phase space of reduced dimensionality (1D in physical space and 3D in velocity space). The code assumes periodic boundary conditions in the spatial coordinate $x \in [0, L]$, while the DF $f(x, \mathbf{v}, t)$ is set equal to zero for $|v| > v_{\max}$ in each velocity direction and at each spatial position.

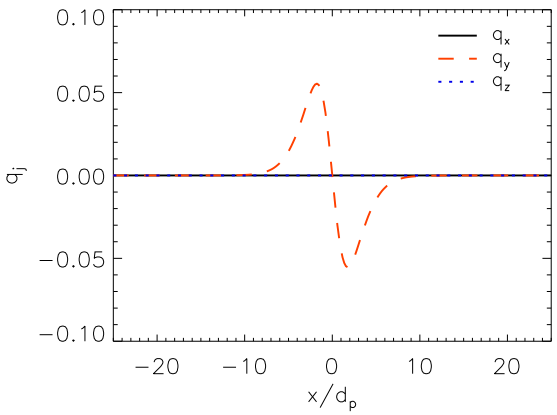

FIG. 7. Heat flux q_x (black solid), q_y (red dashed), and q_z (blue dotted), associated with the proton DF $f_{\mathrm{eq},\perp}$.

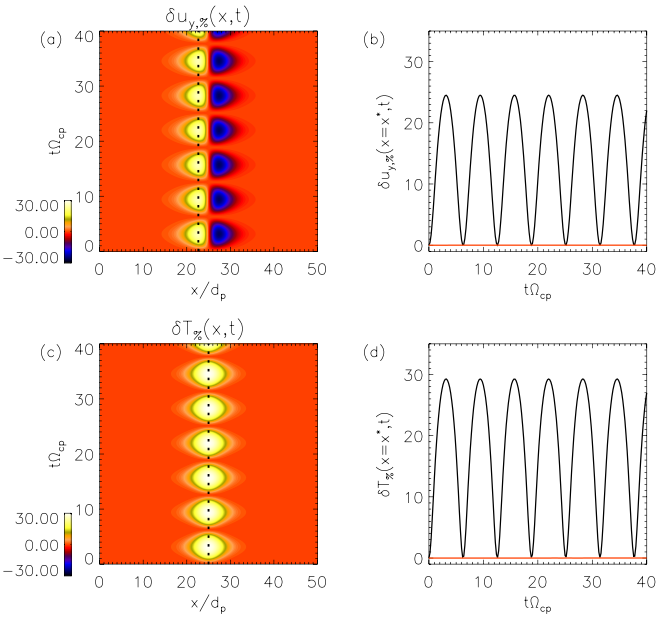

FIG. 8. Top: Contour plot of $\delta u_{y,\%}(x,t)$ for the S1 simulation (a) and temporal profile of $\delta u_{y,\%}(x=x^*,t)$ (b) for the S1 simulation (black) and for the S2 simulation (red), with $x=x^*$ indicated in panel (a) with the black dashed line. Bottom: contour plot of $\delta T_\%(x,t)$ for the S1 simulation (c) and temporal profile of $\delta T_\%(x=x^*,t)$ (d) for the S1 simulation (black) and for the S2 simulation (red), with $x=x^*$ indicated in panel (c) with the black dashed line.

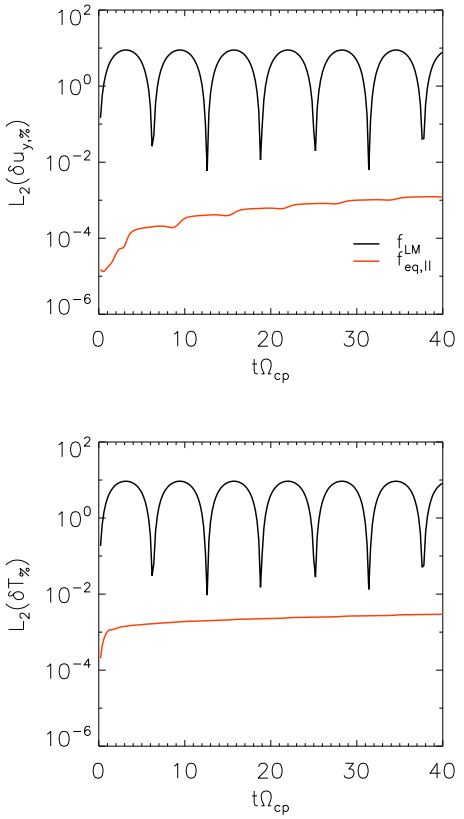

FIG. 9. Temporal evolution of $L_2(\delta u_{y,\%})$ (top row) and $L_2(\delta T_\%)$ (bottom row). In each panel, the black line refers to the $f_{\rm SM}$ DF and the red line to the $f_{\rm eq,||}$ DF.

A. Parallel case

For this case, we discretized the four-dimensional phase space through $N_x = 512$ grid points in the one-dimensional spatial domain and $N_v = 141$ grid points in each velocity direction, while $v_{\rm max} = 7v_{{\rm th},p}$.

We performed two simulations (S1 and S2), keeping fixed the background magnetic field $\mathbf{B}_0 = B_0\mathbf{e}_y$ ($B_0 = 1$ in scaled units) and $\beta_p = 2v_{{\rm th},p}^2/V_A^2 = 4$, but changing the initial proton distribution function. In both simulations, the system dynamics is followed up to a time $t_{\rm max} = 40\Omega_{\rm cp}^{-1}$ and no perturbations are introduced.

We first consider the SMDF $f_{\rm SM}$ [Eq. (6)] as initial condition for the simulation S1. In this case, we set

$$u_0(x) = U_0\left[\tanh\left(\frac{x-L/4}{\Delta x}\right) - \tanh\left(\frac{x-3L/4}{\Delta x}\right) - 1\right] \tag{36}$$

with $U_0 = 2V_A$, $\Delta x = 2.5d_p$, and $L = 100d_p$.

Then, we performed a second simulation S2, using as initial condition the stationary DF $f_{\rm eq,||}$ [Eq. (9)], with

$$U(x-v_z) = U_0\left[\tanh\left(\frac{x-L/4-v_z}{\Delta x}\right) - \tanh\left(\frac{x-3L/4-v_z}{\Delta x}\right) - 1\right], \tag{37}$$

and compared the results of the two simulations. We point out that the expressions in Eqs. (36) and (37) describe a smooth jump in velocity at the position $x = L/4$ along the x direction; this jump has been mirrored at $x = 3L/4$, in order to satisfy the periodic boundary conditions.

As expected, the simulation S1 clearly indicates that the initial distribution SM DF is not an equilibrium and, as a consequence, its velocity moments display an oscillatory behavior with a period equal to the ion gyroperiod. The left column of Fig. 8 displays the contour plots of $\delta u_{y,\%}(x,t) = [u_y(x,t) - u_y(x,0)]/U_0 \times 100$ [Fig. 8(a)] and $\delta T_\%(x,t) = [T(x,t) - T(x,0)]/T^\infty \times 100$ [Fig. 8(c)] in the (x,t) plane, for the simulation S1, where the x range has been set to focus on the left half of the spatial box and where $T^\infty = v_{{\rm th},p}^2 = \beta_p/2 = 2$ in dimensionless units. Significant oscillations (about 30%) are recovered in both u_y and T, localized around the shear.

On the other hand, in the simulations S2 with the DF $f_{\rm eq,||}$, the system remains at equilibrium (no significant oscillations are visible). To better point out the differences between S1 and S2, we considered the temporal profiles of $\delta u_{y,\%}(x,t)$ and $\delta T_\%(x,t)$, evaluated at a fixed spatial position $x = x^*$. The point x^* corresponds to the spatial point where each quantity exhibits the largest amplitude oscillations in simulation S1 [vertical black dashed lines in Figs. 8(a) and 8(c)], with respect to the initial condition, i.e., $\delta u_{y,\%}(x^*,t) = \max_x\{\delta u_{y,\%}(x,t)\}$ and $\delta T_\%(x^*,t) = \max_x\{\delta T_\%(x,t)\}$. These temporal profiles are reported in Figs. 8(b) and 9(d), as black ($f_{\rm SM}$) and red ($f_{\rm eq,||}$) curves, respectively. Here, one can realize that no significant oscillations in the signals are recovered in the case of the DF $f_{\rm eq,||}$, as compared to the case of the SMDF.

To further characterize the differences between the two cases S1 and S2, we also computed the L_2 norm of $\delta u_{y,\%}(x,t)$ and $\delta T_\%(x,t)$, defined as $L_2(g(x,t)) = \sqrt{\int (g-g_0)^2 dx/L}$, with g being a generic function and $g_0 = g(x,0)$. Clearly $L_2(g(x,t))$ is a function of time t. In Fig. 9, we show, in semilogarithmic plot, the temporal evolution of $L_2(\delta u_{y,\%})$ (top row) and $L_2(\delta T_\%)$ (bottom row). As can be appreciated from the plots in this figure, significant oscillations with respect to the initial configuration are present in the case of the SMDF (black solid curves), confirming that this distribution is not a HVM equilibrium. On the other hand, no oscillations are visible for the case of the DF $f_{\mathrm{eq},||}$ (red solid curves), in which the small departure from the initial configuration (about $10^{-4}\%$) is presumably due to the numerical error in the calculation of the velocity moments of $f_{\mathrm{eq},||}$.

B. Perpendicular case

For this case, we discretized the four-dimensional phase space through $N_x = 512$ grid points in the one-dimensional spatial domain and $N_v = 141$ grid points in each velocity direction, while $v_{\max} = 7v_{\mathrm{th},p}$. Two simulations have been performed to compare the SM DF f_{SM} (S3) and the equilibrium DF $f_{\mathrm{eq},\perp}$ (S4), while the background magnetic field is $\mathbf{B}_0 = B_0\mathbf{e}_z$ ($B_0 = 1$ in scaled units) and $\beta_p = 2v_{\mathrm{th},p}^2/V_A^2 = 4$. In both simulations, the system dynamics is followed up to a time $t_{\max} = 40\Omega_{\mathrm{cp}}^{-1}$ and no perturbations are introduced. The initial electric field considered for these simulations is the one given by

$$E(x) = E_0\left[1 - \tanh\left(\frac{x - L/4}{\Delta x}\right) + \tanh\left(\frac{x - 3L/4}{\Delta x}\right)\right] \tag{38}$$

with $E_0 = 1$ (in scaled units), $\Delta x = 2.5d_p$, and $L = 100d_p$. Note that the shear has been mirrored to hold periodic boundary conditions.

As expected, the simulation S3 indicates that the initial distribution SM DF is not an equilibrium. However, with respect to the parallel case, its velocity moment does not display an oscillatory behavior but some propagating structure is also recovered. Left column of Fig. 10 displays the contour plots of $\delta u_{y,\%}(x,t) = [u_y(x,t) - u_y(x,0)]/U_0 \times 100$ [Fig. 10(a)] and $\delta T_\%(x,t) = [T(x,t) - T(x,0)]/T^\infty \times 100$ [Fig. 10(c)] in the (x,t) plane, for the simulation S3, where the x range has been set to focus on the left half of the spatial box and where $T^\infty = v_{\mathrm{th},p}^2 = \beta_p/2 = 2$ in dimensionless units. Disturbances from the equilibrium (about 1–2%) are recovered in both u_y and T, mainly localized around the shear but also showing a propagating structure.

On the other hand, in the simulations S4 with the equilibrium DF, the system remains at equilibrium (oscillations significantly smaller than in S3 are in fact recovered in S4). To better point out the differences between S3 and S4, we considered the temporal profiles of $\delta u_{y,\%}(x,t)$ and $\delta T_\%(x,t)$, evaluated at a fixed spatial position $x = x^*$. The point x^*

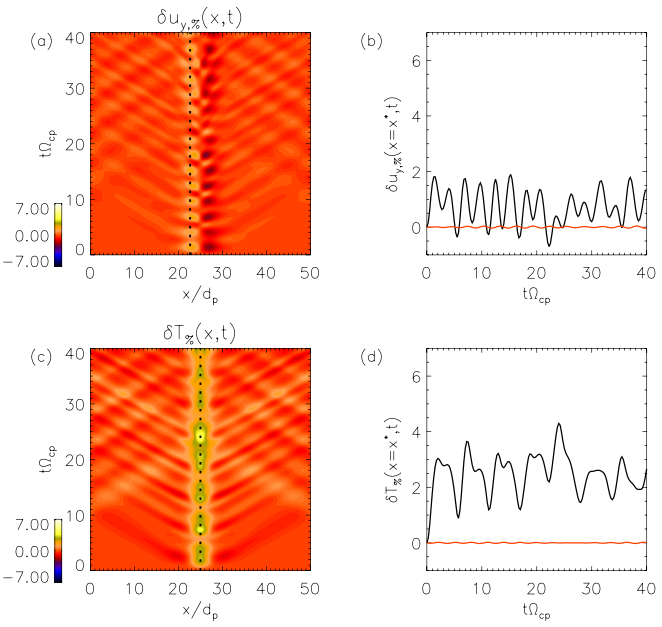

FIG. 10. Top: contour plot of $\delta u_{y,\%}(x,t)$ for the S3 simulation (a) and the temporal profile of $\delta u_{y,\%}(x = x^*,t)$ (b) for the S3 simulation (black) and for the S4 simulation (red), with $x = x^*$ indicated in panel (a) with the black dashed line. Bottom: contour plot of $\delta T_\%(x,t)$ for the S3 simulation (c) and the temporal profile of $\delta T_\%(x = x^*,t)$ (d) for the S3 simulation (black) and for the S4 simulation (red), with $x = x^*$ indicated in panel (c) with the black dashed line.

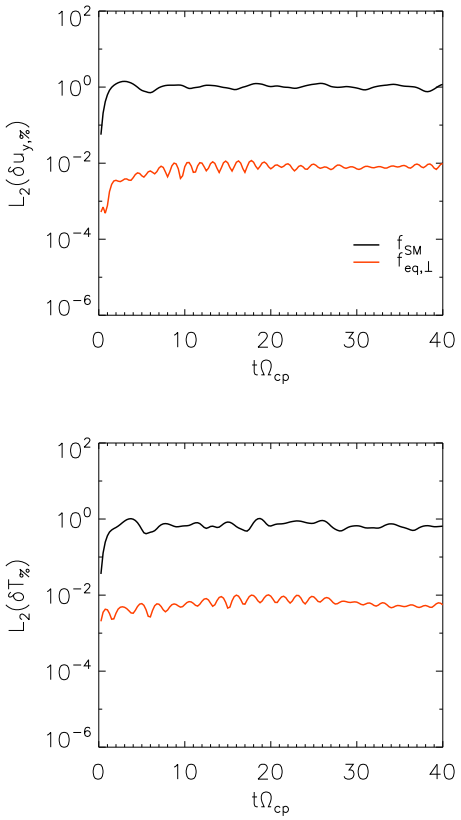

FIG. 11. Temporal evolution of $L_2(\delta u_{y,\%})$ (top row) and $L_2(\delta T_\%)$ (bottom row). In each panel, the black line refers to the f_{SM} DF and the red line to the $f_{\mathrm{eq},\perp}$ DF.

corresponds to the spatial point where each quantity exhibits the largest amplitude oscillations in simulation S3 [vertical black dashed lines in Figs. 10(a) and 10(c)], with respect to the initial condition, i.e., $\delta u_{y,\%}(x^*,t) = \max_x\{\delta u_{y,\%}(x,t)\}$ and $\delta T_\%(x^*,t) = \max_x\{\delta T_\%(x,t)\}$. These temporal profiles are reported in Figs. 10(b) and 10(d), as black and red curves, respectively. Here, one can realize that much smaller oscillations in the signals are recovered in the case of the DF $f_{\mathrm{eq},\perp}$ (red), as compared to the case of the SMDF (black).

To further characterize the differences between the two cases S3 and S4, we also computed the L_2 norm of $\delta u_{y,\%}(x,t)$ and $\delta T_\%(x,t)$, defined as $L_2(g(x,t)) = \sqrt{\int (g-g_0)^2 dx/L}$, being g a generic function and $g_0 = g(x,0)$. Clearly $L_2(g(x,t))$ is a function of time t. In Fig. 11, we show, in semilogarithmic plot, the temporal evolution of $L_2(\delta u_{y,\%})$ (top row) and $L_2(\delta T_\%)$ (bottom row). As can be appreciated from the plots in this figure, significant departures from the initial configuration are present in the case of the SMDF (black solid curves), confirming that this distribution is not a HVM equilibrium. On the other hand, in the case of the DF $f_{\mathrm{eq},\perp}$ (red solid curves) much small departures from the initial configuration (about $10^{-2}\%$) are observed, presumably due to the numerical error in the calculation of the velocity moments of $f_{\mathrm{eq},\perp}$.

VI. SUMMARY AND CONCLUSIONS

In this paper, we have derived exact solutions for the system of hybrid Vlasov-Maxwell equations which represent a stationary shearing flow with a uniform magnetic field directed either parallel or perpendicular to the plasma bulk velocity. Plasmas supporting shearing flows are found in many situations and a kinetic description is necessary whenever the shear width is of the order of kinetic scales, like, for instance, in the case of the Earth's magnetopause [3,20,21,23].

The interest of building up stationary solutions can be related to the problem of describing the propagation and evolution of waves in a plasma with a stable shearing flow. The interaction between waves and the background inhomogeneity associated with the shearing flow moves the wave energy toward small scales, where kinetic effects are more effective. Moreover, the presence of a shearing flow can generate wave coupling, with an energy transfer among different wave modes. It is clear that, in order to properly study wave propagation, it is necessary that the background structure remains stationary; otherwise, a time evolution intrinsic of the background state would superpose to waves, making difficult to single out the wave contribution in the overall time evolution. Another possible application of exact shearing flow solutions can be found in the study of the Kelvin-Helmoholtz instability, which takes place in unstable shearing velocity configurations. In fact, though the turbulent stage following the instability saturation should be quite insensitive to the details of the initial state, only a stationary unperturbed configuration allows us to properly describe the linear stage of the instability. Therefore, in both cases an exact stationary distribution function is preferable to the simpler shifted Maxwellian DF.

Stationary solutions in various configurations have been described in previous studies of the fully kinetic case, i.e., involving the full set of ion and electron Vlasov-Maxwell equations. However, the fully kinetic treatment is quite complex and such solutions have rarely been employed in numerical simulations like, for instance, in investigations of the KH instability. In this respect, the set of hybrid Vlasov-Maxwell equations represents a good compromise, because it correctly describes a plasma at scales of the order of or larger than the ion scales but avoiding the complexity of a fully kinetic treatment. In the framework of Vlasov-Maxwell equations, Cerri *et al.* [39] have developed a method to derive approximately stationary solutions. The solutions presented here situate in the same framework but have the advantage to be exactly stationary.

The starting point of our derivation are previous studies where stationary DFs are derived in the fully kinetic framework (Refs. [34,37]), which we revisited and adapted to the hybrid Vlasov-Maxwell description. In particular, we have examined the special cases in which the magnetic field is uniform and either parallel or perpendicular to the bulk velocity. In the former case, the stationary solution has a simple analytical form which can be directly used in numerical simulations; in the latter case, the explicit construction of the distribution function is obtained through a simple numerical procedure which integrates particle orbits throughout the relevant phase space. In the case of parallel **B**, an isothermal electron fluid have been assumed. In contrast, in the case of perpendicular **B**, a nonuniform electron pressure p_e is necessary in order to satisfy the generalized Ohm's law. As a consequence, an adiabatic equation for the electron fluid has been added to the set of equations. This aspect represents a novelty for the hybrid Vlasov-Maxwell approach, in which an isothermal electron fluid has been routinely assumed.

The main properties of these solutions have been examined, calculating the associated profiles of bulk velocity, temperatures, and heat flux. In the shear region, the ion distribution functions are distorted with respect to shifted Maxwellians, with stronger distortions for more localized shears. In particular, marked anisotropy and agyrotropy in the ion temperature are generated, and none of the DF principal axes is aligned to **B**. Moreover, a nonvanishing heat flux is present, directed in the plane perpendicular to the inhomogeneity direction x. We found that the width of the velocity shear cannot be smaller than ion Larmor radius; this can be justified by considering the ion gyromotion which mixes up single-particle velocities on the scale of the Larmor radius.

The HVM code [40] has been employed to verify to what extent the derived configurations remain stationary when used as initial conditions in numerical simulations. The time behavior has been compared with that obtained in the case of a shifted Maxwellian distribution function. We found that in the case of our solutions the deviation from the initial condition remains much smaller (two orders of magnitude for perpendicular **B** and more than three orders of magnitude for parallel **B**) than in the case of the shifted Maxwellian. The small deviation from exact stationarity of the former case are probably due to numerical errors in the HVM code and, for perpendicular **B**, also in the procedure integrating particle orbits.

We are planning to use these results for studying the problem of Alfvén wave evolution in a shearing flow plasma. Moreover, we are currently working to extend them to the case of an

obliquely directed magnetic field, a configuration commonly observed in the Earth's magnetosphere.

ACKNOWLEDGMENTS

This work has been supported by the Agenzia Spaziale Italiana under the contract ASI-INAF 2015-039-R.O "Missione M4 di ESA: Partecipazione Italiana alla fase di assessment della missione THOR". Authors sincerely thank Prof P. Veltri for his fruitful suggestions and anonymous Reviewers for the positive comments on our work. Numerical simulations here described have been performed on the Newton parallel machine at the University of Calabria (Italy).

APPENDIX A: ANISOTROPY EVALUATION AT THE CENTER OF THE SHEAR IN THE PARALLEL CASE

In this Appendix, we analytically calculate, in the case of the shear parallel to the background magnetic field, the variance matrix for the equilibrium DF $f_{\mathrm{eq},||}$ of Eq. (9). We focus on the case where U represents a shear layer across which the bulk velocity varies from a value $-U_0$ to U_0. In the spatial positions far from the velocity shear, $f_{\mathrm{eq},||}$ reduces to a shifted Maxwellian and then the variance matrix becomes diagonal $\sigma_{ij}^{\infty} = v_{\mathrm{th},p}^2 \delta_{ij}$ and $T_0^{\infty} = T_{||}^{\infty} = T_{\perp}^{\infty}$, where the upper index "∞" identifies values calculated far from the shear layer. We focus the center $x = 0$ of a symmetric shear layer, i.e., $U(k_2)$ is an odd function of k_2, where we expect to find the strongest departures from a Maxwellian. In this case, $u_y(x = 0) = 0$, while the variance matrix is

$$\sigma_{ij}(x=0) = \frac{1}{(2\pi)^{3/2} v_{\mathrm{th},p}^3} \int v_i v_j \exp\left(-\frac{1}{2v_{\mathrm{th},p}^2} \left\{ v_x^2 + \left[v_y + U\left(\frac{v_z}{\Omega_{\mathrm{cp}}}\right)\right]^2 + v_z^2 \right\}\right] d^3\mathbf{v}. \tag{A1}$$

In the large-scale limit $\Delta x \gg \rho_{Lp}$ ($\Delta v \gg v_{\mathrm{th},p}$) and by considering that the typical value for the velocity v_z is $v_{\mathrm{th},p}$, we can retain the first-order Taylor expansion term of $U(v_z/\Omega_{\mathrm{cp}})$: $U(v_z/\Omega_{\mathrm{cp}}) \simeq \omega_0/\Omega_{\mathrm{cp}} v_z$, being $\omega_0 \equiv \frac{dU}{dk_2}|_{k_2=0}$.

Within this approximation, all the integrals involved in Eq. (A1) can be easily calculated and the resulting form is

$$\sigma(x=0) = \begin{bmatrix} v_{\mathrm{th},p}^2 & 0 & 0 \\ 0 & \left(1 + \frac{\omega_0^2}{\Omega_{\mathrm{cp}}^2}\right) v_{\mathrm{th},p}^2 & -\frac{\omega_0}{\Omega_{\mathrm{cp}}} v_{\mathrm{th},p}^2 \\ 0 & -\frac{\omega_0}{\Omega_{\mathrm{cp}}} v_{\mathrm{th},p}^2 & v_{\mathrm{th},p}^2 \end{bmatrix}. \tag{A2}$$

Diagonalizing $\sigma(x = 0)$ implies rotating the DF into the minimum variance frame (MVF). The eigenvalues of $\sigma(x = 0)$, corresponding to the temperatures in the MVF, are $\lambda^{(3)} < \lambda^{(2)} < \lambda^{(1)}$, whose explicit expressions are

$$\lambda^{(3)} = v_{\mathrm{th},p}^2 \left(1 - \frac{\omega_0}{\Omega_{\mathrm{cp}}} \sqrt{1 + \frac{\omega_0^2}{4\Omega_{\mathrm{cp}}^2}} + \frac{\omega_0^2}{2\Omega_{\mathrm{cp}}^2}\right),$$
$$\lambda^{(2)} = v_{\mathrm{th},p}^2,$$
$$\lambda^{(1)} = v_{\mathrm{th},p}^2 \left(1 + \frac{\omega_0}{\Omega_{\mathrm{cp}}} \sqrt{1 + \frac{\omega_0^2}{4\Omega_{\mathrm{cp}}^2}} + \frac{\omega_0^2}{2\Omega_{\mathrm{cp}}^2}\right). \tag{A3}$$

The corresponding eigenvectors are given by

$$\xi^{(3)} = \left(\sqrt{1 + \frac{\omega_0^2}{4\Omega_{\mathrm{cp}}^2}} - \frac{\omega_0}{2\Omega_{\mathrm{cp}}}\right)\mathbf{e}_y + \mathbf{e}_z, \quad \xi^{(2)} = \mathbf{e}_x,$$
$$\xi^{(1)} = -\left(\sqrt{1 + \frac{\omega_0^2}{4\Omega_{\mathrm{cp}}^2}} + \frac{\omega_0}{2\Omega_{\mathrm{cp}}}\right)\mathbf{e}_y + \mathbf{e}_z. \tag{A4}$$

From the above expressions, we can deduce the following information:

(i) At $x = 0$, $\sigma_{xx} = \sigma_{zz}$; therefore the two temperatures in the directions orthogonal to **B** are equal, i.e., the DF is gyrotropic in the LBF at $x = 0$.

(ii) By comparing σ_{ij}^{∞} and $\sigma_{ij}(x = 0)$ in Eq. (A2), we note that, at $x = 0$, σ_{xx} and σ_{zz} keep the same value of σ_{ij}^{∞}. Therefore, at the center of the shear, the perpendicular proton temperature remains constant ($T_{\perp}(x) = T_{\perp}^{\infty}$), while the parallel temperature increases ($T_{||}(x = 0) \geqslant T_{||}^{\infty}$). As a consequence, at $x = 0$ the perpendicular to parallel proton temperature ratio is

$$\frac{T_{\perp}(x=0)}{T_{||}(x=0)} = \frac{1}{1 + \omega_0^2/(2\Omega_{\mathrm{cp}}^2)} < 1, \tag{A5}$$

i.e., the proton parallel temperature is larger than the perpendicular one.

(iii) The eigenvectors $\xi^{(m)}$ ($m = 1,2,3$) give the directions of the principal axes of the DF in the velocity space. Far from the shear layer, the DF is isotropic and the directions of principal axes are arbitrary. At $x = 0$, the principal axis $\xi^{(2)}$ is in the v_x direction, which corresponds to the direction of spatial variation of the bulk velocity **u**, while the other two principal axes $\xi^{(1)}$ and $\xi^{(3)}$ are in the $v_y v_z$ plane. The angle γ between $\xi^{(1)}$ and the v_y axis, which gives the directions corresponding to the maximum width of the DF, is

$$\tan\gamma = -\frac{1}{\sqrt{1 + \frac{\omega_0^2}{4\Omega_{\mathrm{cp}}^2}} + \frac{\omega_0}{2\Omega_{\mathrm{cp}}}}. \tag{A6}$$

In the limit of slowly varying bulk velocity ($\omega_0 \ll \Omega_{\mathrm{cp}}$), we get $\gamma \simeq -45^{\circ}$. Finally, it is worth noting that since the three eigenvalues are all different at $x = 0$, the DF is not gyrotropic with respect to any of the three principal axes in the MVF.

It is interesting to extend the results illustrated above through the numerical evaluation of the temperature in the MVF and in the LBF, for several values of the shear width Δx, where the shear function $U(x)$ is given by Eq. (10). Table I reports the values of $\lambda^{(i)}$ (with $i = 1,2,3$), $T_{||}$, $T_{\perp}$, and γ, at the center of the shear $x = 0$. As expected, in the large-scale limit $\Delta x \gg \rho_{Lp}$, the results obtained numerically are in good accordance with the analytical predictions. By decreasing the width of the shear function Δx, the analytical calculations tend to diverge from numerical evaluations. Note also that as the shear width Δx becomes smaller, stronger anisotropies in the LBF (i.e., bigger $T_{||}$) and in the MVF (i.e., larger ratios between the eigenvalues $\lambda^{(i)}$) are recovered at the center of shear.

TABLE I. Temperatures and characteristic angle of the equilibrium distribution function $f_{\mathrm{eq},||}$.

Δ_x/d_p	Evaluation	λ_1	λ_2	λ_3	$T_\parallel$	$T_\perp$	γ
25	Analytical	2.16	2.00	1.85	2.01	2.00	−43.9
25	Numerical	2.16	2.00	1.85	2.01	2.00	−43.9
2.5	Analytical	4.36	2.00	9.17×10^{-1}	3.28	2.00	−34.1
2.5	Numerical	3.75	2.00	1.08	2.82	2.00	−36.0
0.25	Analytical	1.32×10^{2}	2.00	3.03×10^{-2}	1.30×10^{2}	2.00	−7.02
0.25	Numerical	6.53	2.00	9.09×10^{-1}	5.44	2.00	−26.1

APPENDIX B: STATIONARY SOLUTION IN THE LOCAL APPROXIMATION IN THE PERPENDICULAR CASE

In the present Appendix, we report the evaluation of the equilibrium DF, in the perpendicular case, within the so-called local approximation, i.e., in the simplified case of linearly growing electric field. The single-particle motion is calculated by solving Eqs. (19), in the particular case in which the electric field is linear $E(x) = E_0 + \alpha_0(x - x_0)$, with E_0 and α_0 constant. This profile for the electric field is not fully realistic, since $|E(x)|$ grows without limit for increasing $|x - x_0|$. However, it can be considered as a local approximation of an electric profile $E(x)$ around a given position x_0, being $\alpha_0 = (dE/dx)(x_0)$.

In this case, Eq. (21) reads

$$\frac{d^2x}{dt^2} + \omega^2 x = \frac{e}{m_p}(E_0 - \alpha_0 x_0) + \Omega_{\mathrm{cp}} W_0, \tag{B1}$$

where $\omega^2 = \Omega_{\mathrm{cp}}^2 - e\alpha_0/m_p$. If $\Omega_{\mathrm{cp}}^2 > e\alpha_0/m_p$, Eq. (B1) describes an harmonic oscillator of solution:

$$x(t) = R_0 \sin(\omega t + \varphi) + \frac{1}{\omega^2}\left[\frac{e}{m_p}(E_0 - \alpha_0 x_0) + \Omega_{\mathrm{cp}} W_0\right], \tag{B2}$$

with R_0 and φ being the amplitude and the phase of the motion, respectively. The constant term in Eq. (B2) represents the time-averaged x position, i.e., the guiding center position x_c,

$$x_c = \frac{1}{\omega^2}\left[\frac{e}{m_p}(E_0 - \alpha_0 x_0) + \Omega_{\mathrm{cp}} W_0\right], \tag{B3}$$

and then

$$\begin{aligned} x(t) &= R_0 \sin(\omega t + \varphi) + x_c, \\ v_x(t) &= R_0 \omega \cos(\omega t + \varphi), \\ v_y(t) &= -\Omega_{\mathrm{cp}} x(t) + W_0 = -R_0 \Omega_{\mathrm{cp}} \sin(\omega t + \varphi) + v_{cy}, \end{aligned} \tag{B4}$$

where $v_{cy} = \langle v_y(t)\rangle_t = -\Omega_{\mathrm{cp}} x_c + W_0$. Using Eq. (B3) into the v_{cy} expression, one obtains

$$v_{cy} = -\frac{e}{m_p \Omega_{\mathrm{cp}}^2}(\Omega_{\mathrm{cp}} E_0 + \alpha_0 v_{0y}), \tag{B5}$$

where $v_{0y} = -\Omega_{\mathrm{cp}} x_0 + W_0$ is the particle streamwise velocity component at the position $x = x_0$. Note also that $v_{0y} = v_{cy} + \Omega_{\mathrm{cp}}(x_c - x_0)$. By using these last expressions, one obtains

$$v_{cy} = -\frac{e}{m_p \Omega_{\mathrm{cp}}}[E_0 + \alpha_0(x_c - x_0)] = -c\frac{E(x_c)}{B}. \tag{B6}$$

Hence, the guiding center moves along y with the local $\mathbf{E} \times \mathbf{B}$ drift velocity calculated at the guiding center position x_c. Then, in the local approximation case, the particle orbit in the $v_x v_y$ plane is an ellipse elongated along v_x (v_y) for $\alpha_0 < 0$ ($0 < \alpha_0 < m_p \Omega_{\mathrm{cp}}^2/e$), while it reduces to a circle in the case of uniform electric field $\alpha_0 = 0$. In the case $\alpha_0 \geqslant m_p \Omega_{\mathrm{cp}}^2/e$, $x(t)$ increases linearly or exponentially in time, causing the breakdown of the local approximation, as already noticed in Ref. [35].

Note that if $\alpha_0 = 0$ (i.e., $\omega^2 = \Omega_{\mathrm{cp}}^2$), then $v_x^2 + (v_y - v_{cy})^2 = R_0^2 \omega^2$. Indicating by $t_n = (n\pi - \phi)/\omega$ (n integer) an instant of time when $x(t_n) = x_c$, then $v_x(x = x_c) = v_x(t = t_n) = \pm R_0 \omega$ [Eqs. (B4)]. Hence, $v_x^2 + (v_y - v_{cy})^2 = [v_x(x = x_c)]^2$. The same argument shows that $v_x(x = x_c) = \pm R_0 \omega$ also when the electric field is nonuniform ($\alpha_0 \neq 0$). Then, the energy $\mathcal{E}_0$ [Eq. (27)] is

$$\mathcal{E}_0 = \frac{m_p}{2}\left(R_0^2 \omega^2 + v_z^2\right). \tag{B7}$$

In order to explicitly write the form for $f_{\mathrm{eq},\perp}(x, \mathbf{v})$ [Eq. (31)], we manipulate Eq. (B7) by using Eqs. (B4) and Eq. (B6) and by expressing x_c in terms of the particle position and velocity through Eqs. (B4):

$$\mathcal{E}_0 = \frac{m_p}{2}\left[v_x^2 + \frac{\omega^2}{\left(\Omega_{\mathrm{cp}} - c\alpha_0/B\right)^2}\left[v_y + \frac{c}{B}E(x)\right]^2 + v_z^2\right]. \tag{B8}$$

This expression, which is the argument in the exponential of the DF $f_{\mathrm{eq},\perp}$, suggests that $f_{\mathrm{eq},\perp}$ is a shifted bi-Maxwellian with different temperatures $T_u = T_y$ and $T_{\perp u} = T_{xz}$ parallel to and in the plane perpendicular to the bulk flow, respectively. The temperature ratio is $T_u/T_{\perp u} = (\Omega_{\mathrm{cp}} - c\alpha_0/B)^2/\omega^2$; using the explicit expression for ω we find

$$\frac{T_u}{T_{\perp u}} = 1 - \frac{1}{\Omega_{\mathrm{cp}}}\frac{c\alpha_0}{B} = 1 - \frac{e\alpha_0}{m_p \Omega_{\mathrm{cp}}^2}. \tag{B9}$$

Therefore, $T_u > T_{\perp u}$ ($T_u < T_{\perp u}$) when $E(x)$ decreases (increases) with increasing x. Note that, in order to have a positive temperature T_u, the spatial derivative of the electric field has an upper limit: $\alpha_0 < m_p \Omega_{\mathrm{cp}}^2/e$. This condition is the same which avoids the breakdown of the local approximation in the single-ion dynamics, as found in the previous section. Of course, for a uniform electric field ($\alpha_0 = 0$), we have $T_u = T_{\perp u}$.

By requiring that the uniform density $n^{LA}(x) = n_0$, it can be easily shown that

$$f^{LA}_{\mathrm{eq},\perp}(x,\mathbf{v}) = \frac{n_0}{(2\pi)^{3/2} v^3_{\mathrm{th},p}} \left(\frac{T_{\perp u}}{T_u}\right)^{1/2} \times e^{-\frac{1}{2v^2_{\mathrm{th},p}}\{v_x^2 + \frac{T_{\perp u}}{T_u}[v_y + \frac{c}{B}E(x)]^2 + v_z^2\}}, \tag{B10}$$

which depends on two arbitrary constants n_0 and $v_{\mathrm{th},p}$, while the ratio $T_u/T_{\perp u}$ is given by the equation (B9).

The bulk velocity associated with the DF is $\mathbf{u}^{LA} = \int \mathbf{v}\, f^{LA}_{\mathrm{eq},\perp}\, d^3\mathbf{v}/n^{LA}$. The bulk velocity components u_x^{LA} and u_z^{LA} are both vanishing, while the component $u_y^{LA} = -cE(x)/B$, indicating that the bulk velocity coincides with the local $\mathbf{E}\times\mathbf{B}$ drift velocity.

The considered DF is an exact stationary solution of the HVM equations, Eqs. (1)–(3), with Eq. (4) for the pressure closure. The DF $f^{LA}_{\mathrm{eq},\perp}$ is a stationary solution of the Vlasov equation [Eq. (1)], because it is a function only of the motion constant. The electric field profile is linear and its profile is correctly given by the $\mathbf{u}\times\mathbf{B}$ term in Eq. (3) (then the stationarity holds for an electron pressure p_e constant and uniform). Since the electric field is irrotational, the magnetic field is stationary. Therefore, the considered configuration is an exact stationary solution of the whole set of the HVM equations.

[1] M. Fujimoto, T. Terasawa, T. Mukai, Y. Saito, T. Yamamoto, and S. Kokubun, J. Geophys. Res. **103**, 4391 (1998).

[2] H. Hasegawa, M. Fujimoto, T.-D. Phan, H. Reme, A. Balogh, M. W. Dunlop, C. Hashimoto, and R. TanDokoro, Nature (London) **430**, 755 (2004).

[3] N. Sckopke, G. Paschmann, G. Haerendel, B. U. Sonnerup, S. J. Bame, T. G. Forbes, E. W. Hones, and C. T. Russell, J. Geophys. Res. **86**, 2099 (1981).

[4] R. Bruno and V. Carbone, Liv. Rev. Solar Phys. **10**, 2 (2013).

[5] N. D. Hamlin and W. I. Newman, Phys. Rev. E **87**, 043101 (2013).

[6] S. Chandrasekhar, *Hydrodynamic and Hydromagnetic Stability* (Dover, New York, 1961).

[7] J. Heyvaerts and E. R. Priest, Astron. Astrophys. **117**, 220 (1983).

[8] F. Pucci, M. Onofri, and F. Malara, Astrophys. J. **796**, 43 (2014).

[9] J. V. Hollweg and C. G. Lilliequist, J. Geophys. Res. **83**, 2030 (1978).

[10] E. Kh. Kaghashvili, J. Reader, G. M. Webb, and G. P. Zank, Phys. Plasmas **13**, 112107 (2006).

[11] J. V. Hollweg and E. Kh. Kaghashvili, Astrophys. J. **744**, 114 (2012).

[12] C. L. Vásconez, F. Pucci, F. Valentini, S. Servidio, W. H. Matthaeus, and F. Malara, Astrophys. J. **815**, 7 (2015).

[13] F. Pucci, C. L. Vásconez, O. Pezzi, S. Servidio, F. Valentini, W. H. Matthaeus, and F. Malara, J. Geophys. Res. **121**, 1024 (2016).

[14] F. Valentini, C. L. Vásconez, O. Pezzi, S. Servidio, F. Malara, and F. Pucci, Astron. Astrophys. **599**, A8 (2017).

[15] I. Hofmann, Plasma Phys. **17**, 143 (1975).

[16] G. Einaudi and F. Rubini, Phys. Fluids **29**, 2563 (1986).

[17] X. L. Chen and P. J. Morrison, Phys. Fluids B **2**, 495 (1990).

[18] M. Faganello, F. Pegoraro, F. Califano, and L. Marradi, Phys. Plasmas **17**, 062102 (2010).

[19] L. Chacón, D. A. Knoll, and J. M. Finn, Phys. Lett. A **308**, 187 (2003).

[20] S. H. Chen, M. G. Kivelson, J. T. Gosling, R. J. Walker, and A. J. Lazarus, J. Geophys. Res. **98**, 5727 (1993).

[21] M. G. Kivelson and S.-H. Chen, in *The Magnetopause: Surface Waves and Instabilities and their Possible Dynamical Consequences*, edited by P. Song, B. U. Ö. Sonnerup, and M. F. Thomsen, Geophysical Monograph Series (AGU, Washington, DC, 1995), Vol. 90, p. 257.

[22] D. H. Fairfield, A. Otto, T. Mukai, S. Kokubun, R. P. Lepping, J. T. Steinberg, A. J. Lazarus, and T. Yamamoto, J. Geophys. Res. **105**, 21159 (2000).

[23] M. Faganello and F. Califano, J. Pkasma. Phys. **83**, 535830601 (2017).

[24] F. Malara, G. Einaudi, and A. Mangeney, J. Geophys. Res. **94**, 11813 (1989).

[25] Y. Matsumoto and M. Hoshino, Geophys. Res. Lett. **31**, L02807 (2004).

[26] T. K. M. Nakamura, D. Hayashi, M. Fujimoto, and I. Shinohara, Phys. Rev. Lett. **92**, 145001 (2004).

[27] Y. Matsumoto and M. Hoshino, J. Geophys. Res. **111**, A05213 (2006).

[28] Y. Matsumoto and K. Seki, J. Geophys. Res. **112**, A06223 (2007).

[29] M. Faganello, F. Califano, and F. Pegoraro, Phys. Rev. Lett. **100**, 015001 (2008).

[30] P. Henri, S. S. Cerri, F. Califano, F. Pegoraro, C. Rossi, M. Faganello, O. Šebek, P. M. Trávníček, P. Hellinger, J. T. Frederiksen *et al.*, Phys. Plasmas **20**, 102118 (2013).

[31] C. Rossi, F. Califano, A. Retinó, L. Sorriso-Valvo, P. Henri, S. Servidio, F. Valentini, A. Chasapis, and L. Rezeau, Phys. Plasmas **22**, 122303 (2015).

[32] F. Di Mare, L. Sorriso-Valvo, A. Retinò, H. Hasegawa, and F. Malara, (unpublished).

[33] D. Cai, L. R. O. Storey, and T. Neubert, Phys. Fluids B: Plasma Phys. **2**, 75 (1990).

[34] G. Ganguli, Y. C. Lee, and P. J. Palmadesso, Phys. Fluids **31**, 823 (1988).

[35] K.-I. Nishikawa, G. Ganguli, Y. C. Lee, and P. J. Palmadesso, Phys. Fluids **31**, 1568 (1988).

[36] S. M. Mahajan and R. D. Hazeltine, Phys. Plasmas **7**, 1287 (2000).

[37] V. Roytershteyn and W. Daughton, Phys. Plasmas **15**, 082901 (2008).

[38] H. Karimabadi, V. Roytershteyn, M. Wan, W. H. Matthaeus, W. Daughton, P. Wu, M. Shay, B. Loring, J. Borovsky, E. Leonardis, S. C. Chapman, and T. K. M. Nakamura, Phys. Plasmas **20**, 012303 (2013).

[39] S. S. Cerri, P. Henri, F. Califano, D. Del Sarto, M. Faganello, and F. Pegoraro, Phys. Plasmas **20**, 112112 (2013).

[40] F. Valentini, P. Travnicek, F. Califano, P. Hellinger, and A. Mangeney, J. Comput. Phys. **225**, 753 (2007).

[41] S. Servidio, F. Valentini, F. Califano, and P. Veltri, Phys. Rev. Lett. **108**, 045001 (2012).
[42] W. H. Matthaeus, S. Oughton, K. T. Osman, S. Servidio, M. Wan, S. P. Gary, M. A. Shay, F. Valentini, V. Roytershteyn, H. Karimabadi, and S. C. Chapman, Astrophys. J. **790**, 155 (2014).
[43] L. Franci, A. Verdini, L. Matteini, S. Landi, and P. Hellinger, Astrophys. J. Lett. **804**, L39 (2015).
[44] S. Servidio, F. Valentini, D. Perrone, A. Greco, F. Califano, W. H. Matthaeus, and P. Veltri, J. Plasma Phys. **81**, 325810107 (2015).
[45] F. Valentini, D. Perrone, S. Stabile, O. Pezzi, S. Servidio, R. De Marco, F. Marcucci, R. Bruno, B. Lavraud, J. De Keyser *et al.*, New J. Phys. **18**, 125001 (2016).
[46] S. S. Cerri, F. Califano, F. Jenko, D. Told, and F. Rincon, Astrophys. J. Lett. **822**, L12 (2016).
[47] O. Pezzi, T. N. Parashar, S. Servidio, F. Valentini, C. V. Vásconez, Y. Yang, F. Malara, W. H. Matthaeus, and P. Veltri, Astrophys. J. **834**, 166 (2017).
[48] S. S. Cerri, F. Pegoraro, F. Califano, D. Del Sarto, and F. Jenko, Phys. Plasmas **21**, 112109 (2014).
[49] D. Del Sarto, F. Pegoraro, and F. Califano, Phys. Rev. E **93**, 053203 (2016).
[50] S. S. Cerri, arXiv:1804.02109 [physics.space-ph].
[51] D. Del Sarto and F. Pegoraro, Mon. Not. R. Astron. Soc. **475**, 181 (2018).
[52] E. G. Harris, Nuovo Cimento **23**, 115 (1962).
[53] N. A. Krall and A. W. Trivelpiece, *Principle of Plasma Physics* (McGraw-Hill, New York, 1973).
[54] S. Naitou, S. Tokuda, and T. Kamiura, J. Comput. Phys **38**, 265 (1980).
[55] F. Valentini, D. Perrone, and P. Veltri, Astrophys. J. **739**, 54 (2011).
[56] F. Valentini, S. Servidio, D. Perrone, F. Califano, W. H. Matthaeus, and P. Veltri, Phys. Plasmas **21**, 082307 (2014).
[57] S. S. Cerri, S. Servidio, and F. Califano, Astrophys. J. Lett. **846**, L18 (2017).
[58] O. Pezzi, T. N. Parashar, S. Servidio, F. Valentini, C. V. Vásconez, Y. Yang, F. Malara, W. H. Matthaeus, and P. Veltri, J. Plasma Phys. **83**, 905830105 (2017).
[59] O. Pezzi, F. Malara, S. Servidio, F. Valentini, T. N. Parashar, W. H. Matthaeus, and P. Veltri, Phys. Rev. E **96**, 023201 (2017).